Simulating Jellyfish Galaxies: A Case Study for a Gas-rich Dwarf Galaxy

Jaehyun Lee, Taysun Kimm, Jérémy Blaizot, Harley Katz, Wonki Lee,
Yun-Kyeong Sheen, Julien Devriendt, Adrianne Slyz

HAL Id: insu-03711523
https://insu.hal.science/insu-03711523

Submitted on 2 Jul 2022

Simulating Jellyfish Galaxies: A Case Study for a Gas-rich Dwarf Galaxy

Jaehyun Lee[1] , Taysun Kimm[2] , Jérémy Blaizot[3] , Harley Katz[4] , Wonki Lee[2] , Yun-Kyeong Sheen[5] ,
Julien Devriendt[4] , and Adrianne Slyz[4]

[1] Korea Institute for Advanced Study, 85, Hoegi-ro, Dongdaemun-gu, Seoul 02455, Republic of Korea
[2] Department of Astronomy, Yonsei University, 50 Yonsei-ro, Seodaemun-gu, Seoul 03722, Republic of Korea; tkimm@yonsei.ac.kr
[3] Univ Lyon, Univ Lyon1, Ens de Lyon, CNRS, Centre de Recherche Astrophysique de Lyon UMR5574, F-69230 Saint-Genis-Laval, France
[4] Astrophysics, University of Oxford, Denys Wilkinson Building, Keble Road, Oxford, OX1 3RH, UK; syncphy@gmail.com
[5] Korea Astronomy and Space Science Institute, 776 Daedeokdae-ro, Yuseong-gu, Daejeon 34055, Republic of Korea

Abstract

We investigate the formation of jellyfish galaxies using radiation-hydrodynamic simulations of gas-rich dwarf galaxies with a multiphase interstellar medium (ISM). We find that the ram-pressure-stripped (RPS) ISM is the dominant source of molecular clumps in the near wake within 10 kpc from the galactic plane, while in situ formation is the major channel for dense gas in the distant tail of the gas-rich galaxy. Only 20% of the molecular clumps in the near wake originate from the intracluster medium (ICM); however, the fraction reaches 50% in the clumps located at 80 kpc from the galactic center since the cooling time of the RPS gas tends to be short owing to the ISM–ICM mixing ($\lesssim 10$ Myr). The tail region exhibits a star formation rate of 0.001–0.01 $M_\odot$ yr^{-1}, and most of the tail stars are born in the stripped wake within 10 kpc from the galactic plane. These stars induce bright Hα blobs in the tail, while Hα tails fainter than 6×10^{38} erg s^{-1} kpc^{-2} are mostly formed via collisional radiation and heating due to mixing. We also find that the stripped tails have intermediate X-ray-to-Hα surface brightness ratios ($1.5 \lesssim F_{\rm X}/F_{\rm H\alpha} \lesssim 20$), compared to the ISM ($\lesssim 1.5$) or pure ICM ($\gg 20$). Our results suggest that jellyfish features emerge when the ISM from gas-rich galaxies is stripped by strong ram pressure, mixes with the ICM, and enhances the cooling in the tail.

1. Introduction

Ram pressure stripping, characterized by tails, is a key mechanism that accelerates galaxy evolution in cluster environments (Gunn et al. 1972; Davies & Lewis 1973; Boselli & Gavazzi 2006). Observations have revealed multiphase tails in H I (Kenney et al. 2004; Oosterloo & van Gorkom 2005; Chung et al. 2007, 2009; Scott et al. 2010, 2012, 2018), Hα (Gavazzi et al. 2001; Cortese et al. 2006, 2007; Sun et al. 2007; Yagi et al. 2007, 2010; Fumagalli et al. 2014; Boselli et al. 2016; Poggianti et al. 2017; Sheen et al. 2017), and even in X-ray bands (Finoguenov et al. 2004; Wang et al. 2004; Machacek et al. 2005; Sun & Vikhlinin 2005; Sun et al. 2006, 2010), demonstrating that the interstellar medium (ISM) is efficiently removed from a galaxy by ram pressure and eventually dispersed by interactions with the intracluster medium (ICM). Although ram pressure stripping is believed to quench star formation on long timescales (Koopmann & Kenney 2004a, 2004b), various empirical and numerical studies have revealed other complicated effects of ram pressure stripping on galaxies (e.g., Grishin et al. 2021; Mun et al. 2021). For example, ram pressure can enhance star formation in satellite galaxies by compressing the ISM in the early stages of the infall (e.g., Steinhauser et al. 2012; Vulcani et al. 2018). Features associated with young stars are observed in some ram-pressure-stripped (RPS) wakes (e.g., Owers et al. 2012; Ebeling et al. 2014; Fumagalli et al. 2014; Rawle et al. 2014;

Poggianti et al. 2016; Jáchym et al. 2017, 2019; Sheen et al. 2017; George et al. 2018), denoting the presence of dense molecular clouds surrounded by hot gas with temperatures higher than several million kelvin.

Indeed, extraplanar and tail CO emission is observed from RPS galaxies (Jáchym et al. 2014, 2017, 2019; Verdugo et al. 2015; Lee et al. 2017; Lee & Chung 2018; Moretti et al. 2018). Some even have massive molecular clouds of $M_{\rm H_2} \sim 10^9\,M_\odot$ in their tails (Jáchym et al. 2017, 2019; Moretti et al. 2018), with a hint of star formation (see Jáchym et al. 2017, 2019, for further details). Given that the lifetime of dense molecular clouds is typically less than 10 Myr in an idealized environment without ICM winds (e.g., Blitz & Shu 1980; Vázquez-Semadeni et al. 2005) and the orbital velocity of a cluster satellite galaxy (i.e., wind velocity in wind tunnel experiments) is typically less than a few thousand kilometers per second, the molecular clouds observed tens of kiloparsecs away from the midplane of a galactic disk may have been formed in situ, rather than directly stripped from the main body of a galaxy (Jáchym et al. 2017).

Many attempts have been made to understand the impact of ram pressure stripping on galaxies using numerical approaches. Disk stripping processes have been intensively examined for ICM winds with various properties (Schulz & Struck 2001; Vollmer et al. 2001, 2006; Roediger & Brüggen 2006, 2007, 2008; Jáchym et al. 2009). Furthermore, studies have explored the role of magnetic fields in ram pressure stripping (Ruszkowski et al. 2014; Shin & Ruszkowski 2014; Tonnesen & Stone 2014; Ramos-Martínez et al. 2018). Star formation in RPS disks and tails is another topic that has been investigated using numerical simulations (Schulz & Struck 2001; Vollmer et al. 2001; Bekki & Couch 2003; Kapferer et al. 2008, 2009;

Kronberger et al. 2008; Steinhauser et al. 2012; Tonnesen & Bryan 2012). However, studies examining the complicated interplay between ram pressure and the multiphase ISM driven by star formation and stellar feedback are lacking. Lee et al. (2020, hereafter L20) investigated the impact of varying ICM winds on the multiphase disk of a dwarf-sized galaxy using a suite of radiation-hydrodynamic (RHD) simulations. They showed that mild ICM winds with ram pressure $P_{ram}/k_B = 5 \times 10^4 \, K \, cm^{-3}$ gradually strip the multiphase ISM from the galaxy while enhancing star formation in the disk at least for 400 Myr after the interaction with the winds. In contrast, strong ICM winds with $P_{ram}/k_B = 5 \times 10^5 \, K \, cm^{-3}$, mimicking ram pressure at a cluster center (e.g., Jung et al. 2018), quickly remove most of the ISM, suppressing star formation on a timescale of ~ 100 Myr. However, no star formation occurs in the RPS tails owing to the absence of dense molecular clouds, even when the radiative cooling rates are enhanced by the adoption of a low ICM temperature of $T = 10^6$ K.

Although a limited number of cases have been observed thus far, RPS galaxies with massive molecular clouds in their tails are known to be gas-rich in their disks (Jáchym et al. 2017, 2019; Moretti et al. 2018). Half of these galaxies appear to be located close to a cluster center ($r_c < 300$ kpc), perhaps experiencing strong ram pressure. Although gas-rich galaxies are likely to be more resilient to ram pressure owing to their high column density (Gunn et al. 1972) and strong ISM pressure sustained by the active star formation (e.g., Ostriker et al. 2010; Kim & Ostriker 2018), the strong ram pressure can remove a large amount of the ISM from the galaxies. Such stripped gas may contribute to the accumulation of cold gas in the galaxy tails via radiative cooling (e.g., Armillotta et al. 2016, 2017; Gronke & Oh 2018). The stripped ISM can also be mixed with the ICM (Franchetto et al. 2021), forming Hα and X-ray tails that are different from the pure ISM or ICM (Poggianti et al. 2019; Sun et al. 2021). Motivated by these observational and theoretical results, we hypothesize that the abundant ISM stripped from a galaxy could facilitate molecular clump formation in the RPS tails of gas-rich galaxies.

This study aims to understand the formation process of galaxies with multiphase gas and young stars in their tails, called jellyfish features, via RHD simulations. Section 2 describes the RHD method and the initial conditions of our simulations. Section 3 examines the formation of molecular clouds and stars in the disks and tails of simulated galaxies and compares the findings with observed cases. Section 4 demonstrates the correlation between Hα emission and star formation activity in an RPS tail. In Section 5, we discuss the origin of the Hα–X-ray surface brightness (SB) relation observed in the RPS tails. Finally, Section 6 summarizes the major findings.

2. Simulations

In this section, we describe our RHD simulations, including the initial conditions of the simulated galaxies and the ICM wind, and the computation of the Hα emissivity.

2.1. Code

We use RAMSES-RT (Rosdahl et al. 2013; Rosdahl & Teyssier 2015), which is an RHD version of the adaptive mesh refinement code RAMSES (Teyssier 2002). RAMSES-RT adopts

the HLLC (Toro et al. 1994) and the particle-mesh method (Guillet & Teyssier 2011) to solve the Euler equations and the Poisson equations, respectively. The RAMSES-RT version used herein includes a modified photochemistry model for tracing the formation and destruction of molecular hydrogen (Katz et al. 2017; Kimm et al. 2017), as well as the nonequilibrium chemistry and cooling of six chemical species: H I, H II, He I, He II, He III, and e$^-$ (Rosdahl et al. 2013; Rosdahl & Teyssier 2015). Atomic metal cooling at $T \gtrsim 10^4$ K is computed using the CLOUDY cooling model (Ferland et al. 1998), whereas fine-structure line cooling at $T \lesssim 10^4$ K is computed using the cooling model of Rosen & Bregman (1995). Radiative cooling induced by molecular hydrogen is also included (Hollenbach & McKee 1979; Halle & Combes 2013).

The spectral energy distributions of stars are obtained from the Binary Population and Spectral Synthesis model (BPASS version 2.0; Eldridge et al. 2008; Stanway et al. 2016) based on an initial mass function (IMF) with slopes of -1.3 for stellar masses between 0.1 and 0.5 $M_\odot$ and -2.35 for stellar masses between 0.5 and 100 $M_\odot$ (Kroupa 2001). We utilize a star formation model that computes star formation efficiency based on the local thermo-turbulent condition (Kimm et al. 2017). Star formation is allowed in cells with hydrogen number density n_H higher than $100 \, cm^{-3}$, but most stellar particles form in cells with $n_H > 1000 \, cm^{-3}$; this is because our thermo-turbulent star formation scheme requires gravitationally bound structures (see L20 for details).

The simulation box is covered with 256^3 root cells (level 8), which are adaptively refined to resolve the local thermal Jeans length by at least eight cells until it reaches the maximum refinement level of 14. The corresponding maximum resolution is 18 pc.

Our simulations include various stellar feedback mechanisms, i.e., photoionization, radiation pressure exerted by photons at wavelengths ranging from UV to IR (Rosdahl et al. 2013; Rosdahl & Teyssier 2015), and Type II supernova (SN) explosions (Kimm et al. 2015). Additionally, the SN frequency is increased by a factor of five. Note that such a boost is necessary to reproduce the stellar mass growth and the UV luminosity functions of galaxies at $z \geq 6$ (e.g., Rosdahl et al. 2018; Garel et al. 2021) or the mass fraction of stars in Milky Way−like galaxies (Li et al. 2018). Finally, the metal yield from SNe is neglected to allow us to distinguish the contributions from the ISM and ICM to the gas in a cell. Further details about the physical ingredients used in the simulations are presented in L20.

2.2. Initial Conditions

To investigate the conditions for jellyfish galaxy formation, we adopt the same structural properties of the disk galaxy that were employed in L20 (FaceWind10), except that we alter the amount of disk gas mass. The galaxies initially have a stellar mass of $2.10 \times 10^9 \, M_\odot$ with a bulge-to-total mass ratio of $f_{bulge} \approx 0.17$ and are embedded in a dark matter halo of mass $M_{halo} = 10^{11} \, M_\odot$ and virial radius $R_{vir} = 89$ kpc, as in Rosdahl et al. (2015). The disk gas metallicities are set to $Z_{ISM} = 0.75 \, Z_\odot$, where the solar metallicity is $Z_\odot = 0.0134$ (Asplund et al. 2009). The initial gas mass of the Face-Wind10 galaxy (L20) is $M_{gas} = 1.75 \times 10^9 \, M_\odot$, and we adopt five times more gas mass in the NoWind_rich and FaceWind10_rich runs ($M_{gas} = 8.75 \times 10^9 \, M_\odot$). As can
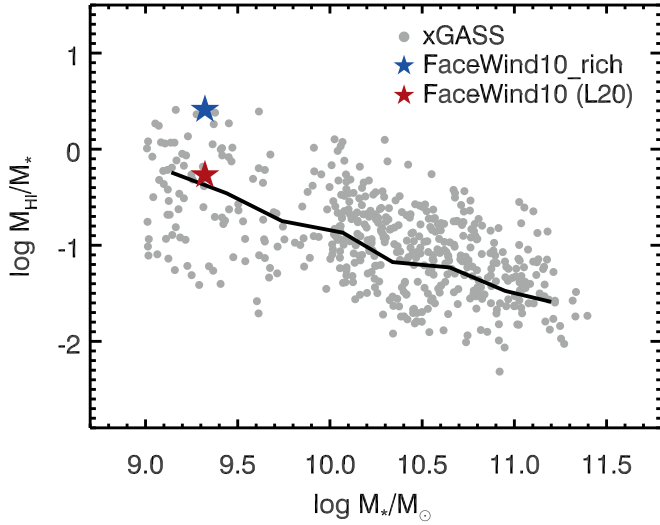
Figure 1. Initial gas fraction of the simulated galaxies (blue star: `FaceWind10_rich`; red star: `FaceWind10`). Gray circles show the H I fraction-to-stellar mass relation of the local galaxies from the xGASS survey (Catinella et al. 2018). The black solid line denotes the average of the logarithmic H I mass fractions weighted by the local galaxy stellar mass function (see Catinella et al. 2018, for further details).

be seen in Figure 1, these initial gas masses represent a galaxy with a normal or high gas fraction, compared to the local galaxies in the xGASS survey (Catinella et al. 2018).

Starting from these initial conditions, the gas-rich galaxy (`FaceWind10_rich`) is evolved for 250 Myr to ensure that it enters a quasi-equilibrium state before it interacts with the ICM wind. At 250 Myr, the mass of neutral, molecular, and ionized hydrogen and stars in the galaxy, measured in the cylindrical volume of a radius of $r = 12$ kpc and a height of $z = \pm 3$ kpc, is $M_{\rm H\,I} = 1.93 \times 10^9\,M_\odot$, $M_{\rm H_2} = 4.90 \times 10^8\,M_\odot$, $M_{\rm H\,II} = 3.37 \times 10^8\,M_\odot$, and $M_* = 3.22 \times 10^9\,M_\odot$, respectively. For comparison, before interaction with the ICM wind, the `FaceWind10` galaxy has $M_{\rm H\,I} = 6.43 \times 10^8\,M_\odot$, $M_{\rm H_2} = 2.62 \times 10^8\,M_\odot$, $M_{\rm H\,II} = 1.27 \times 10^8\,M_\odot$, and $M_* = 2.18 \times 10^9\,M_\odot$. Thus, compared to the `FaceWind10` galaxy in L20, the `FaceWind10_rich` galaxy has 2.7 times more cold gas mass ($M_{\rm H\,I+H_2}$) or 1.8 times higher cold gas fraction ($M_{\rm H\,I+H_2}/M_*$) before the first interaction with the ICM wind.

We impose an ICM wind from one side of the box after 150 Myr and define this epoch as $t = 0$. The ICM wind has a temperature of $T_{\rm ICM} = 10^7$ K, metallicity of $Z_{\rm ICM} = 0.004 \approx 0.3\,Z_\odot$, and velocity of $v_{\rm ICM} = 1000\,{\rm km\,s^{-1}}$, based on the observations of nearby clusters (e.g., Tormen et al. 2004; Hudson et al. 2010; Urban et al. 2017). In our fiducial model (`FaceWind10_rich`), given its initial velocity, the ICM wind starts influencing the galaxy at $t \approx 135$ Myr, after the galaxy enters a quasi-equilibrium state. The wind density is set as $n_{\rm H,ICM} = 3 \times 10^{-3}\,{\rm cm^{-3}}$ to mimic the ram pressure that a satellite galaxy would experience in the central regions of clusters with $M_{200} \sim 10^{14.8}\,M_\odot$ at $z = 0$ (Jung et al. 2018, see their Figure 10). The simulations are run up to $t = 366$ Myr (or 516 Myr in total including the initial relaxation phase). The ICM wind of `FaceWind10` in L20 is identical to that of `FaceWind10_rich`. For comparison, we also run a control simulation without an ICM wind (`NoWind_rich`). Table 1 summarizes the input parameters of the simulations used in this study.
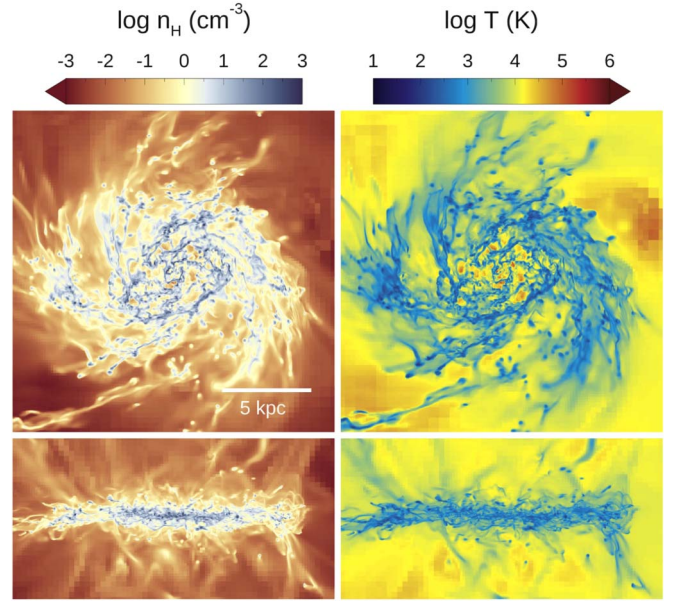

Figure 2. Projected views of the gaseous disk of the simulated galaxy. The panels display the face-on (top) and edge-on (bottom) views of density-weighted distribution of the hydrogen number density (left) and temperature (right) from the `NoWind_rich` galaxy at $t = 135$ Myr, i.e., the moment at which the ICM wind starts influencing the galaxy.

Table 1
Initial Parameters of the Simulations

Model	$n_{\rm H,ICM}$ (cm^{-3})	$v_{\rm ICM}$ (km s^{-1})	$P_{\rm ram}/k_{\rm B}$ (K cm^{-3})	$M_{\rm gas}$ ($10^9\,M_\odot$)
NoWind_rich	10^{-6}	0	0	8.75
FaceWind10_rich	3×10^{-3}	10^3	5×10^5	8.75
FaceWind10 (L20)	3×10^{-3}	10^3	5×10^5	1.75

Note. From left to right, each column indicates the model name, ICM density ($n_{\rm H,ICM}$), ICM velocity ($v_{\rm ICM}$), ram pressure of the wind, and initial gas mass in the disk of the simulation.

Figure 2 shows the projected distribution of the hydrogen number density and temperature of the galaxy at $t = 135$ Myr in `NoWind_rich`. Due to vigorous stellar feedback led by active star formation in the gas-rich disk, the gaseous disk is thicker and more feathery than that with a normal gas fraction (see Figure 1 of L20).

2.3. Computing Hα Emission with Dust

Warm ionized gas with $T \sim 10^4$ K emits Hα photons with $\lambda = 6562.8$ Å via the recombination of ionized hydrogen with a free electron. The number of Hα photons emitted from a cell per unit time during the recombination process is

$$N_{\rm H\alpha,rec} = n_{\rm e} n_{\rm H\,II} \epsilon^B_{\rm H\alpha}(T) \alpha_B(T) \times (\Delta x)^3, \qquad (1)$$

where $n_{\rm e}$ and $n_{\rm H\,II}$ are the electron and ionized hydrogen number densities in the cell, respectively, T is the temperature of the gas in the cell, $\alpha_B(T)$ is the case B recombination coefficient, $\epsilon^B_{\rm H\alpha}(T)$ is the recombination fraction yielding Hα photons at T, and $(\Delta x)^3$ is the volume of each cell. The recombination fraction $\epsilon^B_{\rm H\alpha}$ is computed using the following fit to the recombination coefficients given by
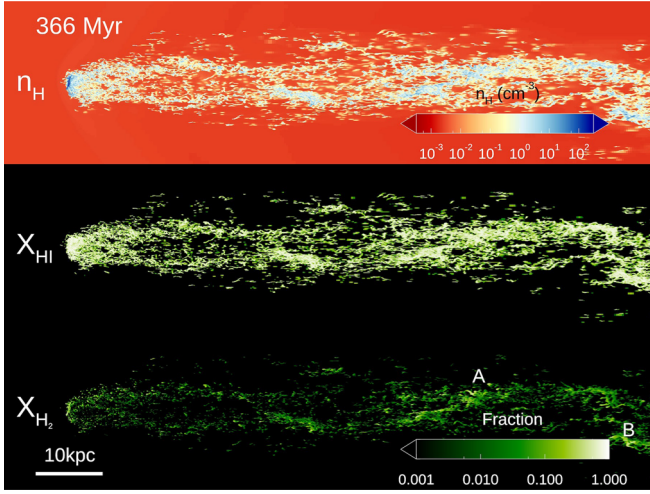
Figure 3. Density-weighted projections of hydrogen number density (n_H), fraction of neutral hydrogen ($X_{H\,I}$), and fraction of molecular hydrogen (X_{H_2}) from the `FaceWind10_rich` run at $t = 366$ Myr. The fractions are the mass ratios to the total hydrogen mass. Tail molecular clouds with $n_H > 100$ cm^{-3} are marked by A and B in the bottom panel.

Storey & Hummer (1995):

$$\epsilon_{H\alpha}^B(T) = 8.176 \times 10^{-8} - 7.461$$
$$\times 10^{-3} \log T_4 + 0.451 \, T_4^{-0.1013}, \quad (2)$$

where $T_4 \equiv T/10^4$ K. The recombination coefficient α_B is taken from Hui & Gnedin (1997) as

$$\alpha_B(T) = 2.753 \times 10^{-14} \text{ cm}^3 \text{ s}^{-1}$$
$$\frac{\lambda_{H\,I}^{1.5}}{[1.0 + (\lambda_{H\,I}/2.740)^{0.407}]^{2.242}}, \quad (3)$$

where $\lambda_{H\,I} = 2 \times 157{,}807$ K$/T$.

Another process that yields Hα photons is collisional excitation of H I by free electrons. The number of Hα photons emitted from a cell per unit time via collisional excitation is given by

$$N_{H\alpha,col} = n_e \, n_{H\,I} \, C_{i,j}^e(T) \times (\Delta x)^3, \quad (4)$$

where $n_{H\,I}$ is the number density of neutral hydrogen and $C_{i,j}^e(T)$ is the electron collisional excitation rate coefficient for a Maxwellian electron velocity distribution at T. Following H. Katz et al. (2022, in preparation), the electron collisional excitation rate coefficient is computed as

$$C_{i,j}^e(T) = \frac{8.628 \times 10^{-6} \text{ cm}^3 \text{ s}^{-1}}{T^{1/2}} \frac{\Upsilon_{i,j}(T)}{\omega_i} \exp\left(\frac{-E_{i,j}}{k_B T}\right), \quad (5)$$

where ω_i is the statistical weight of energy level i, $E_{i,j}$ is the energy difference between levels i and j, k_B is the Boltzmann constant, and $\Upsilon_{i,j}(T)$ is the thermally averaged collision strength, which can be theoretically obtained as follows:

$$\Upsilon_{i,j}(T) = \int_0^\infty \Omega_{i,j} \exp\left(-\frac{E_j}{k_B T}\right) d\left(\frac{E_j}{k_B T}\right), \quad (6)$$

where E_j is the energy of the scattered electron relative to the energy level j and $\Omega_{i,j}$ is the dimensionless collisional strength that is symmetric ($\Omega_{i,j} = \Omega_{j,i}$; Dere et al. 1997). To compute $\Upsilon_{i,j}(T)$ for the Hα photon emission from electron collisional

excitation of H I, we use the CHIANTI database (Del Zanna et al. 2021, version 10), which provides the scaled effective electron collision strength based on the rules formulated by Burgess & Tully (1992). We compute the collisional emission under a case B approximation for collisions up to energy level 5 (Dere et al. 2019). In practice, the collisional emissivity of Hα can be approximated as a function of temperature (H. Katz et al. 2022, in preparation):

$$\epsilon_{H\alpha,col} = \frac{6.01 \times 10^{-19}}{T^{0.230}} \exp\left(\frac{-8.13 \times 10^4}{T^{0.938}}\right) \text{ erg cm}^3 \text{ s}^{-1}. \quad (7)$$

Note that we neglect the collisional Hα emission from a cell if its net cooling timescale is less than three times the local simulation time step to avoid spurious emission from cells where the cooling time is underresolved.[6]

The amount of dust in a cell is modeled following the prescription of Laursen et al. (2009):

$$n_d = (n_{H\,I} + f_{ion} \, n_{H\,II}) \, Z/Z_0, \quad (8)$$

where n_d is a pseudo−number density of dust grains, f_{ion} is the fraction of dust remaining in ionized gas, Z is the gas metallicity, and Z_0 is the averaged metallicity of a galaxy. In this study, we adopt $f_{ion} = 0.01$ and $Z_0 = 0.01$ (Laursen et al. 2009). Dust attenuation is then applied by reducing the intrinsic line emission by $\exp(-\tau_d(\lambda))$, where $\tau_d(\lambda)$ ($= \sum_i n_{d,i} \Delta x_i \sigma_{d,H}(\lambda)$) is the sum of dust optical depth along a sight line. The effective cross section per hydrogen at wavelength λ ($\sigma_{d,H}(\lambda)$) is taken from Weingartner & Draine (2001), assuming Large Magellanic Cloud−type dust.

3. Impact of Ram Pressure on Star Formation Activity

Figure 3 shows the distribution of gas density, the fraction of neutral hydrogen, and the fraction of molecular hydrogen in the `FaceWind10_rich` galaxy with prominent tail structures at the end of the simulation ($t = 366$ Myr). In this section, we investigate how the tails develop in gas-rich galaxies after encountering strong ICM winds and how stars form in the tail regions. We also compare the cases of a gas-rich galaxy in an isolated environment (`NoWind_rich`) and an RPS galaxy with a typical gas fraction (`FaceWind10` from L20).

3.1. Star Formation in the Disk

Figure 4 shows the birthplace of individual stellar particles in the `NoWind_rich` (top panel) and `FaceWind10_rich` (bottom panel) runs at $z > 0.1$ kpc between 0 Myr $\leqslant t \leqslant 366$ Myr, where z is the vertical distance from the midplane of the disk. The galactic midplane is defined from the center of galaxy stellar mass in the XY plane, and the radial distance (R) is measured using the cylindrical coordinate system. For comparison, the stars born before the wind is launched (i.e., $t < 0$ Myr) are shown in gray. In `NoWind_rich`, no stellar particles form at $z > 3$ kpc after $t = 135$ Myr,

---

[6] We restart a snapshot at 366 Myr from the `FaceWind10_rich` run by adopting a Courant number of 0.08 (an order of magnitude smaller than the typical value) and confirm that the collisional Hα luminosity is converged by imposing the condition that there is no collisional radiation if $\tau_{cool} < 3 \, \Delta t_{sim}$. Here we estimate the cooling time τ_{cool} by dividing the thermal energy by the cooling rate in each cell.
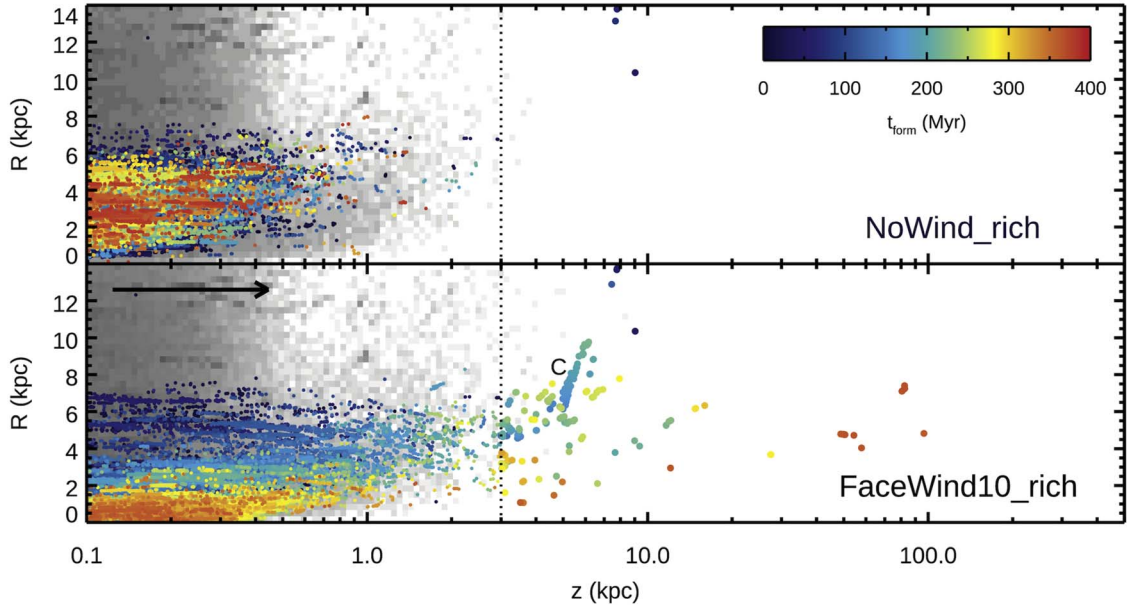
Figure 4. Birthplace of stars in cylindrical coordinates in the `NoWind_rich` (top panel) and `FaceWind10_rich` (bottom panel) runs. The coordinate systems are defined from the center of stellar mass, and the galactic midplane is chosen in the *XY* plane. The black arrow in the bottom panel indicates the ICM wind direction. The color code denotes the birth epoch of each stellar particle formed after the ICM wind is launched. The gray shades depict the distribution of stellar particles formed before $t = 0$. The vertical dotted line indicates the height ($z = 3$ kpc) above which no stars form after the wind starts influencing the galaxy ($t > 135$ Myr) in the `NoWind_rich` run. We thus adopt $z = 3$ kpc as the separation between the disk and tail. A significant star formation event in the tail region is marked as C.

corresponding to the epoch at which the strong ICM winds start influencing the `FaceWind10_rich` galaxy. Thus, we define the vertical distance of 3 kpc as the separation between the tail and disk stellar populations. Notably, this scale is comparable to the height of the cylindrical volume enclosing more than 95% of the total cold gas (H I+H$_2$) in the gas-rich galaxy.

We find that star formation in the disk is significantly suppressed under strong ram pressure. In Figure 4, while no particular trend is seen in the radial distribution of new stars in the `NoWind_rich` galaxy, the star-forming region shrinks over time in the `FaceWind10_rich` galaxy because of the stripping of the gaseous disk. We estimate the truncation radius (r_t) using the Gunn–Gott criterion (Gunn et al. 1972) by balancing the gravitational restoring force and ram pressure as $\rho_{ICM} v_{ICM}^2 = -\Sigma(r_c)\partial\Phi(r_c, z)/\partial z$, where $\Phi(r_c, z)$ is the gravitational potential obtained from the sum of the matter components (gas, stars, and dark matter) at a radius r_c and a vertical height z in the cylindrical coordinate system, and $\Sigma(r_c)$ is a gas column density at r_c. The column density is measured from the gas component in the concentric shell with a radius $[r_c, r_c + \Delta r]$ and a height $|z| < 3$ kpc, following the definition of the galactic disk in this study. Next, we compute the gravitational restoring force and ram pressure at a disk thickness of $H = \sqrt{\int \rho z^2 dV / \int \rho dV}$, where ρ is the total matter density (gas, stars, and dark matter) and dV is the cylindrical volume element inside the scale length (l) of the cold gas (H I+H$_2$) disk. The disk thickness, scale length, and truncation radius just after the galaxy encounters the ICM wind ($t \approx 140$ Myr) are $H = 0.416$ kpc, $l = 2.56$ kpc, and $r_t = 2.74$ kpc, respectively. Indeed, we confirm that the gaseous disk at $r > r_t$ is largely ($\sim 90\%$) stripped within 125 Myr. Accordingly, almost all stars (99.4%) form inside the truncation radius at $t > 250$ Myr, and some stellar particles form outside the disk when the disk is first perturbed by the ICM wind ($t \sim 150$–250 Myr).

Figure 5 compares the star formation rates (SFRs) in the disk and tail of the three simulations. Once the strong ICM wind begins to influence the simulated galaxies, the star formation in the disk decreases by $\approx 40\%$ every 100 Myr in the `FaceWind10_rich` and `FaceWind10` galaxies. During 135 Myr $< t <$ 366 Myr, the stellar mass in the `FaceWind10_rich` galaxy increases by $1.22 \times 10^8 M_\odot$, which is less than half the stellar mass formed in the `NoWind_rich` galaxy ($\Delta M_* = 3.01 \times 10^8 M_\odot$) during the same period. The star formation activity is suppressed from outside to inside owing to disk truncation. In contrast, as illustrated in Figure 6, star formation is enhanced in the central region ($r < 1$ kpc) by a factor of ≈ 2 owing to the compression of the ISM. The same trend is observed in the galaxy with a normal gas fraction. In contrast, the disk in the `NoWind_rich` galaxy maintains its SFR profile during the entire time period. This demonstrates that the strong ram pressure efficiently quenches the star formation not only in galaxies with a typical gas fraction but also in a gas-rich galaxy by stripping away the gaseous disk in extreme environments, such as the central region of galaxy clusters.

3.2. Star Formation in the Tail

Figure 4 shows that stars form in the stripped wake of the gas-rich galaxy at $z > 3$ kpc. By the end of the simulation, a total stellar mass of $3.16 \times 10^5 M_\odot$ is produced in the tail ($z > 3$ kpc), with $\sim 90\%$ of it located in 3 kpc $< z <$ 10 kpc. The bluish trail marked by C ($R \approx 6$–10 kpc and $z \approx 5$–6 kpc) in the bottom panel of Figure 4 is particularly noteworthy. The formation time of each stellar particle is tightly correlated with the distance from the galactic center, indicating that the stellar particles are formed inside clouds moving outward. We visually confirm from the tail region close to the galaxy that the ISM gas is first stripped away from the disk and then collapses to form giant clouds at $z \sim 5$ kpc, which in turn
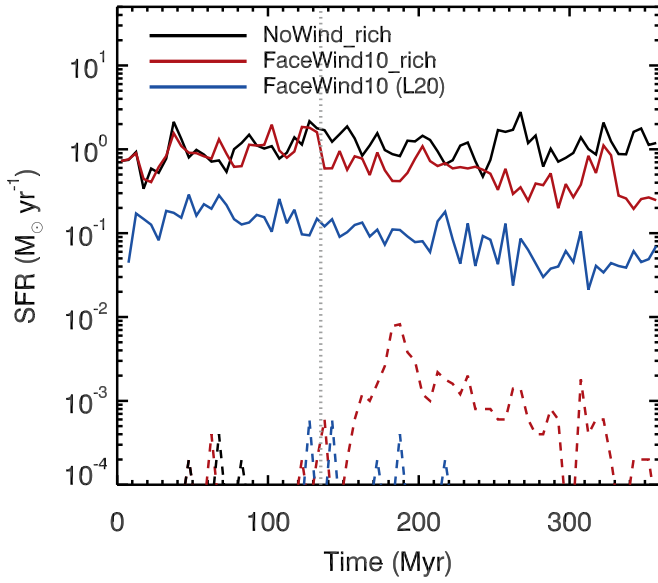
Figure 5. SFR evolution in the galactic disk (solid lines) and in the tail (dashed lines). The three different colors represent the `NoWind_rich` (black), `FaceWind10_rich` (red), and `FaceWind10` (blue, L20) runs. The gray vertical dotted line at $t = 135$ Myr denotes the epoch at which the wind front reaches the galaxy. In the `FaceWind10_rich` run, the SFRs in the galactic disk decrease once the ICM wind encounters the disk, whereas the star formation in the tail commences and is most noticeable ≈ 50 Myr from the start of the ICM–ISM interaction (i.e., $t \approx 185$ Myr).
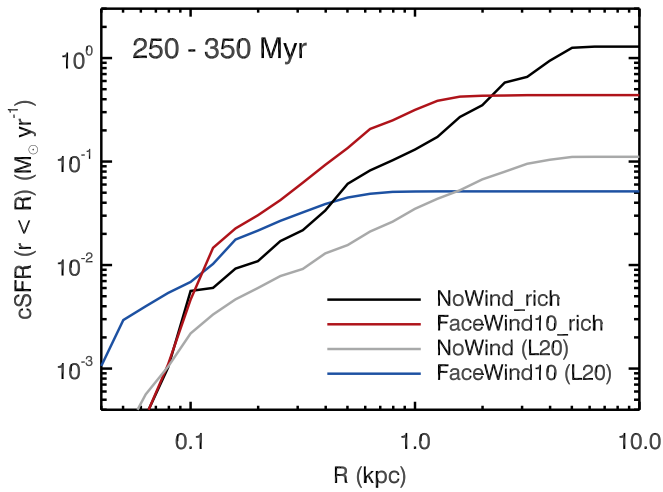
Figure 6. Cumulative SFRs (cSFRs) as a function of the cylindrical radius of the disk (R), averaged over $250 \text{ Myr} \leqslant t \leqslant 350 \text{ Myr}$. For comparison with `FaceWind10`, we also plot the cSFR of the `NoWind` galaxy of L20 (gray solid line). The galaxies interacting with the ICM wind (red and blue lines) show enhanced star formation in the central region ($R \lesssim 1$ kpc), but it is suppressed at $R \gtrsim 1$ kpc, compared to their counterparts without winds (black and gray lines).

produce two adjacent stellar clumps of mass of $M_\star = 3.0 \times 10^4 M_\odot$ and $1.3 \times 10^4 M_\odot$.

The gas-rich galaxy exhibits a remarkably higher SFR in its stripped wake than the `FaceWind10` galaxy (dashed lines in Figure 5). Its SFR is still lower than the galactic SFRs, but it increases to 0.001–$0.01 M_\odot \text{ yr}^{-1}$ for ~ 50 Myr once the disk encounters the wind. The SFR in the tail is comparable to that of D100 ($dM_\star/dt = 3.9 \times 10^{-3} M_\odot \text{ yr}^{-1}$), a spiral galaxy with $M_* \sim 2 \times 10^9 M_\odot$ experiencing strong ram pressure stripping
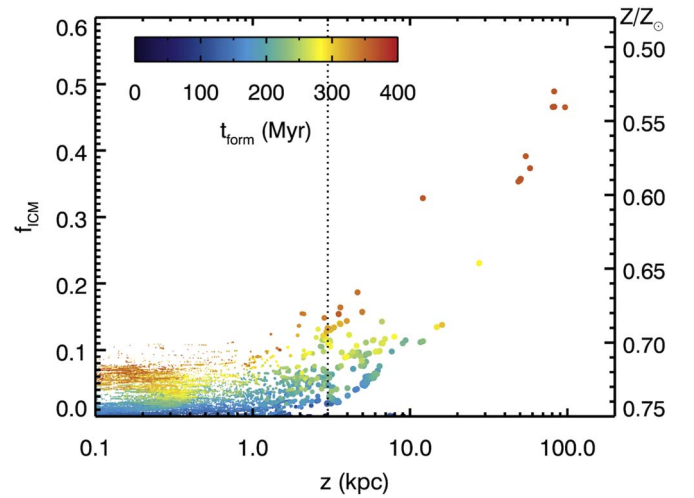

Figure 7. Fraction of the ICM-origin gas (f_{ICM}) in each stellar particle as a function of vertical distance (z). f_{ICM} is estimated from the metallicity of stellar particles (Z) by differentiating the contribution from the ISM ($Z_{ISM} = 0.75 Z_\odot$) and ICM ($Z_{ICM} = 0.3 Z_\odot$). The color code denotes the formation epochs of stellar particles, and the vertical dotted line indicates the separation between tail and disk. The increasing trend of f_{ICM} indicates that more distant stars form in the clouds that have mixed more efficiently with the cooled ICM.

in the Coma Cluster (Jáchym et al. 2017), albeit with some differences (see Section 3.4). In contrast, no significant star formation occurs in the stripped wake of the `FaceWind10` galaxy.

Figure 7 hints at different origins for the stars formed in the stripped wake and the disk. We remind the readers that the fraction of gas cooled from the ICM can be directly inferred from the stellar metallicity $Z_\star$, since the initial metallicities of the ISM and ICM are fixed ($Z_{ISM} = 0.75 Z_\odot$ and $Z_{ICM} = 0.3 Z_\odot$, respectively) and the metal enrichment due to SNe is turned off. The ICM-origin fraction of a gas cell or a stellar particle with a metallicity Z is computed as $f_{ICM} = 1 - f_{ISM} = (Z_{ISM} - Z)/(Z_{ISM} - Z_{ICM})$. First, more than 97.5% of the new stars in the disk ($z < 3$ kpc) show f_{ICM} lower than 7.6%. At a fixed vertical distance, stars formed at a later epoch have slightly higher f_{ICM}, indicating that a fraction of the ICM wind continuously accretes onto the central disk. Indeed, the column density of the ICM that encounters the disk during the interaction ($n_{H,ICM} v_{ICM} \Delta t$) amounts to a few percent of the typical N_H in the central disk, or roughly 10% of that in the outer gaseous disk ($r \approx 3 R_{1/2}$). However, the increase of f_{ICM} is not dramatic (<0.1) during $t \sim 150$–366 Myr, indicating that a dense ISM is largely shielded from strong ICM winds. This is likely due to the strong turbulent pressure afforded by the interplay between gravity and stellar feedback, as demonstrated by L20. Second, new stars formed at $z = 3$–10 kpc also primarily originate from the ISM. The ICM fraction that contributes to new star particle formation in the tail is less than 20% ($f_{ICM} < 0.2$). On the other hand, the new stars located far behind the galactic plane ($z > 10$ kpc) form in clouds well mixed with the ICM, and only half of the stellar mass originates from the stripped ISM. The mass of stars formed in the distant tail is considerably lower ($M_\star = 2.40 \times 10^4 M_\odot$) than that formed near the galactic plane, but their presence implies that molecular clouds can form in the RPS tail. In contrast, dense clouds with $n_H > 100 \text{ cm}^{-3}$ do not form in the stripped wake of the `FaceWind10` galaxy at $t > 200$ Myr.
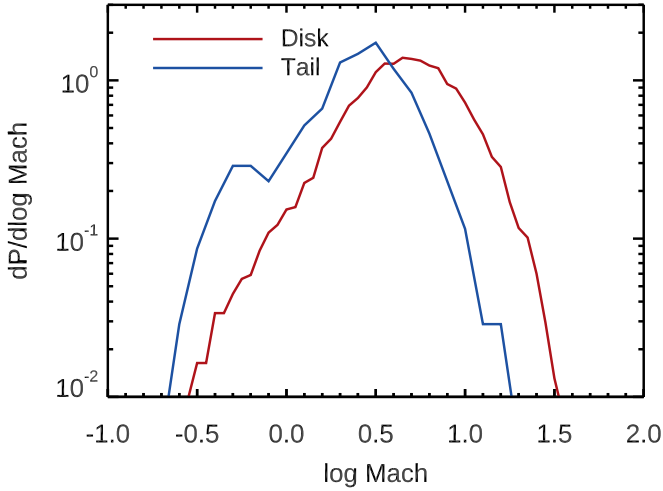
Figure 8. Turbulent properties of star-forming candidate cells with $n_H > 100$ cm^{-3} in the disk (red) and tail region (blue). The turbulent Mach number is estimated from the six immediate neighboring cells (see text). Note that star-forming regions in the RPS tail are not more turbulent than the galactic disk.

Figure 9. Fraction of the molecular hydrogen stemming from the ICM as a function of vertical distance at $t = 366$ Myr. The color code denotes the hydrogen number density of the molecular gas in a cell. The symbol size indicates the mass of the molecular gas ranging from 150 $M_\odot$ to $2.7 \times 10^4\,M_\odot$. Only the gas cells with $n_H > 1$ cm^{-3} are displayed. Two prominent molecular clouds with $n_H > 100$ cm^{-3} in the tail region ($z > 3$ kpc, demarcated by the vertical dotted line) are marked by A and B, which are also presented in the bottom panel of Figure 3.

We then examine the dynamical state of tail gas clouds in the `FaceWind10_rich` galaxy by measuring the turbulent Mach number. The turbulent Mach number is computed as $\mathcal{M} = \sigma_{gas}/c_s$, where $\sigma_{gas} = |\partial v/\partial x|\Delta x$ is the turbulent velocity measured using the six immediate neighboring cells, and $c_s = \sqrt{\gamma P_{th}/\rho_{gas}}$ is the local sound speed with an adiabatic index of $\gamma = 5/3$, where ρ_{gas} and P_{th} are the gas density and thermal pressure of the cell of interest, respectively. Figure 8 shows the probability density function of the Mach number distribution ($dP/d\log\mathcal{M}$) of gas cells with $n_H > 100$ cm^{-3} in all the snapshots at $t > 135$ Myr, after which the ICM wind influences the gas-rich galaxy. The majority of the dense cells in the disk and tail have Mach numbers higher than 1, indicating the presence of supersonic turbulence. Unlike the naive expectation that the dense gas in the tail may be significantly perturbed by the ICM wind, the dense gas with $n_H > 100$ cm^{-3} in the tail region is in fact slightly less turbulent than that of the disk. Furthermore, the dense gases in the disk and tail exhibit virial parameter[7] distributions similar to each other. These results demonstrate that the tail has a quiescent star formation activity not because its dense clouds are more turbulent than those in the galactic disk but simply because the gas reservoir for star formation is limited in the tail (e.g., $M_{dense,disk} = 1.73 \times 10^8\,M_\odot$ versus $M_{dense,tail} = 2.16 \times 10^6\,M_\odot$ for gas with $n_H > 100$ cm^{-3} at $t = 250$ Myr).

3.3. Origin of the Star-forming Gas in the Tail

In the `FaceWind10_rich` galaxy, the cold dense ISM is disrupted by the interaction with the ICM. However, an RPS tail may provide a more favorable environment for gas cooling and molecular gas formation than the galactic disk vicinity, as the tail contains few young stars that emit ionizing photons. Furthermore, as hinted in Figure 7, the mixing with the stripped ISM in the tail increases the density and metallicity of the ICM, leading to enhanced gas cooling. In such environments, the formation of dust and molecular hydrogen is likely to become
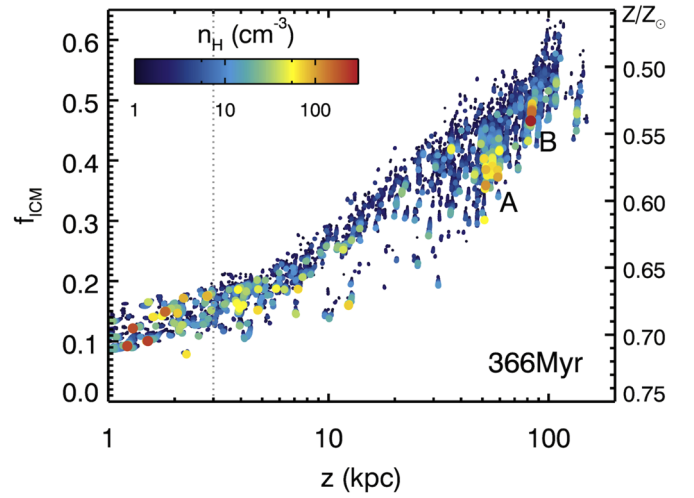
---

[7] The virial parameter for individual cells is computed as $\alpha_{vir} \equiv 2|E_{kin}|/E_{pot} \approx 5(\sigma_{gas}^2 + c_s^2)/\pi\rho_{gas}G\Delta x^2$.

efficient (see, e.g., Section 2.1.3 of L20, and references therein).

As shown in Figure 3, the stripped wake clearly comprises molecular clouds that sometimes have $n_H > 100$ cm^{-3} (marked as A and B in the bottom panel). Figure 9 further shows that more distant cells contain more molecular hydrogen originating from the ICM. In the vicinity of the disk, the dominant source of the molecular hydrogen ($\sim$90%) is the ISM, and the rest is that coming from the ICM owing to strong ram pressure. However, once the stripped tail is pushed out to 100 kpc from the galaxy, approximately half of the total molecular gas is cooled from the ICM, consistent with recent observational and numerical findings (Franchetto et al. 2021; Tonnesen & Bryan 2021). Two dense regions at $z \approx 60$ kpc (marked as A) and $z \approx 80$ kpc (marked as B) are particularly interesting, as they develop near the end of the simulation ($t = 366$ Myr). Specifically, a portion of the stripped ISM is spread over a large volume of $\sim(10$ kpc)^3, and this partially ionized, intermediate-density ($n_H \sim 1$ cm^{-3}), and porous medium collapses to form dense clumps.

To understand the formation of molecular hydrogen in the RPS tail, we compute the net cooling timescale $t_{cool,net} \equiv E_{int}/\mathcal{C}_{net}$, where E_{int} is the internal energy. The net cooling rate ($\mathcal{C}_{net}$) is computed by considering the heating due to local radiation fields and cooling due to atomic and metallic species, as in the simulation. Figure 10 illustrates the net cooling time of the gas in the RPS tails in `FaceWind10` and `FaceWind10_rich`. In the tail region of the `FaceWind10` galaxy, the typical density and temperature of the ionized ($f_{H\,II} > 0.5$) gas, which can potentially cool and contribute to the total H I, are low ($n_H \approx 0.01$ cm^{-3}) and hot ($T \approx 9 \times 10^6$ K), respectively. The median net cooling time is $t_{cool,net} \approx 600$ Myr, which is twice the simulation duration. A portion of the gas with $f_{ICM} \sim 0.5$–0.7 has a short cooling time of $t_{cool,net} < 1$ Myr, but its total mass is not significant. This explains why few dense molecular clouds form in the tail of the galaxy with a normal gas fraction.
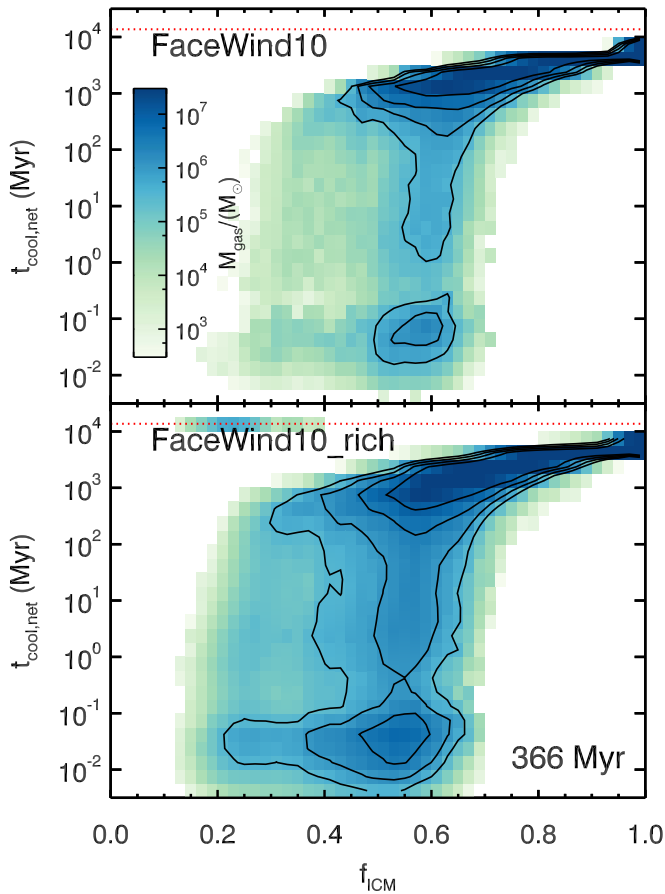
Figure 10. Net cooling time of the gas in the RPS tail as a function of f_{ICM} at $t = 366$ Myr. The top panel shows the distribution for FaceWind10, whereas the FaceWind10_rich case is shown in the bottom. We measure $t_{cool,net}$ for the cells with H II mass fractions higher than 0.5 to focus on potentially cooling regions. The net cooling time is computed by considering the cooling and heating due to local radiation. Gas cells being heated or cells with the cooling time greater than the Hubble time (red dotted lines), i.e., $t_{cool,net} > 13.7$ Gyr, are all indicated as $t_{cool,net} = 13.7$ Gyr. The color code indicates the total gas mass in each bin.

In contrast, in the FaceWind10_rich galaxy, the amount of the ionized ISM-origin gas in the tail is approximately 20 times larger than that in the FaceWind10 galaxy. The presence of abundant warm ionized gas results in a substantial peak at $t_{cool,net} < 1$ Myr, making the $t_{cool,net}$ distribution clearly bimodal. The median density and temperature of these cells in the tail are also higher ($n_H \approx 0.1$ cm^{-3}) and cooler ($T \approx 4 \times 10^4$ K), respectively, and the cooling times are significantly shorter than those in FaceWind10. In such conditions, the gas freely collapses within 100–200 Myr. For comparison, pure ICM gas cannot cool or collapse within a Gyr. Thus, our numerical experiments support the observational interpretation that molecular clouds form in situ in the distant RPS tails (Jáchym et al. 2017, 2019; Moretti et al. 2018) by increasing the tail gas density because of the mixing and enhanced cooling due to the stripped ISM.

3.4. Comparisons with Observations

Several observations have measured the amount and distribution of molecular gas in the wakes of RPS galaxies using CO emission lines. Verdugo et al. (2015) detected molecular gas amounting to $\sim 10^6 M_\odot$ in the RPS tail of NGC 4388 in the Virgo Cluster. In contrast, ESO 137-001 possesses

a large amount of molecular hydrogen of mass $\sim 10^9 M_\odot$ in its tail (Jáchym et al. 2014), and a similar amount of molecular hydrogen is present in the tail of D100 in the Coma Cluster (Jáchym et al. 2017). Furthermore, Moretti et al. (2018) found $M_{H_2} \sim 10^9 M_\odot$ of molecular hydrogen in the tails of four massive jellyfish galaxies with stellar mass of $\sim 3 \times 10^{10-11} M_\odot$. ESO 137-002 is one more case recently reported to have abundant molecular gas ($\sim 5.5 \times 10^9 M_\odot$) in its disk and tail (Laudari et al. 2022). The amount of molecular hydrogen detected in the tail of ESO 137-002 is $M_{H_2} \sim 2.2 \times 10^8 M_\odot$. These galaxies with massive molecular tails are observed either to currently have gas-rich disks or to have possessed them until recently (Jáchym et al. 2014, 2017, 2019; Moretti et al. 2018; Laudari et al. 2022); thus, the amount of gas in the infalling galaxies is likely a key property for forming jellyfish features, which is consistent with our experiment wherein only the FaceWind10_rich galaxy develops the prominent RPS tails.

Of those, D100 in the Coma Cluster is probably the most comparable example to the FaceWind10_rich galaxy. D100 has a stellar mass of $2.1 \times 10^9 M_\odot$ (Yagi et al. 2010), which is similar to that of the FaceWind10_rich galaxy ($M_* = 3.3 \times 10^9 M_\odot$). Since the orbital velocity of D100 is $v \sim 3000$–4000 km s^{-1} and the ICM density is $\sim 3.3 \times 10^{-27}$ g cm^{-3} at the projected distance of 240 kpc (Jáchym et al. 2017), the ram pressure currently exerted on D100 is also very strong (6–10 times larger than that of FaceWind10_rich). Moreover, since the tail of D100 is nearly perpendicular to the direction to the cluster center, D100 is likely passing through its pericenter, suggesting that it has been exposed to strong ram pressure for ~ 200 Myr.[8] However, note that the molecular hydrogen mass ($4.8 \times 10^8 M_\odot$) and SFRs ($2.3 M_\odot$ yr^{-1}) of the D100 disk are larger by a factor 5–6 than those of the FaceWind10_rich galaxy (Jáchym et al. 2017). This indicates that D100 might have been even more gas-rich than the FaceWind10_rich galaxy before falling into the Coma Cluster.

We also compare the properties of the RPS tails of D100 and the FaceWind10_rich galaxy. Hα luminosity suggests that the total SFR in the tail of D100 is $dM_\star/dt = 3.9 \times 10^{-3} M_\odot$ yr^{-1} (Jáchym et al. 2017), which is larger than the averaged SFR obtained in the simulated tail of the FaceWind10_rich galaxy ($dM_\star/dt = 1.2 \times 10^{-3} M_\odot$ yr^{-1}) at $t = 135$–366 Myr. The difference of a factor of three in the SFRs may be attributed to different gas masses in the tail. Although the observations of the D100 tail reveal a considerable amount of molecular hydrogen ($M_{H_2} \sim 10^9 M_\odot$; Jáchym et al. 2017), the observed tail is found to be H I deficient (Bravo-Alfaro et al. 2000, 2001). In contrast, the tail of the FaceWind10_rich galaxy comprises a molecular hydrogen mass of $1.3 \times 10^8 M_\odot$ with $M_{H_2}/M_{H I} \sim 0.1$ at $t = 366$ Myr. Interestingly, $M_{H_2}/M_{H I}$ steadily increases over time in FaceWind10_rich, due to the rapid increase in H$_2$, compared to the increase of neutral hydrogen. Yet the extreme

---

[8] We infer the orbital motion of D100 assuming a dark matter halo of mass $M_{200} = 2.7 \times 10^{15} M_\odot$ and a radius of $R_{200} = 2.9$ Mpc, estimated for the Coma Cluster (Kubo et al. 2007). We adopt the Navarro–Frenk–White profile (Navarro et al. 1996) with a concentration index of $c = 9.4$ (Łokas & Mamon 2003). The ICM density is computed using a β-profile with parameters derived from the Coma Cluster (Mohr et al. 1999; Fossati et al. 2012). This simple calculation suggests that, with the pericenter velocity of 4000 km s^{-1}, D100 is likely to have been exposed to a ram pressure that is comparable to or stronger than that in FaceWind10_rich in the last ~ 200 Myr.
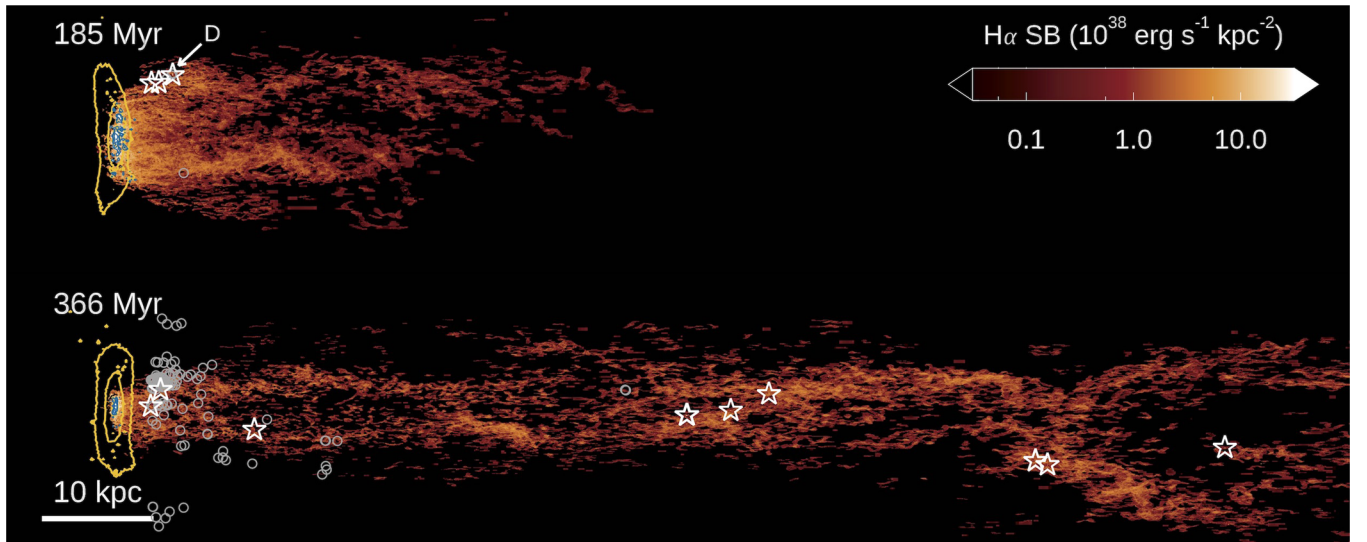
Figure 11. Dust-obscured Hα map of the gas-rich galaxy (`FaceWind10_rich`) at $t = 185$ (top) and 366 Myr (bottom). Yellow and blue contours show the distribution of all stars and the stars younger than 20 Myr in the galactic disk, respectively. White star symbols mark the locations of stellar particles younger than 20 Myr in the RPS tail ($z > 3$ kpc). Older stellar particles formed in the tail at 100 Myr $< t_{form} < 344$ Myr are denoted as open gray circles. A clump of young stars generating bright Hα cores ($F_{H\alpha} > 10^{41}$ erg s^{-1} kpc^{-2}) in the stripped wake is marked as D in the top panel.

H$_2$/H I ratio in the D100 tail is still difficult to explain based on the results of our simulations. Jáchym et al. (2019) also showed that ESO 137-001 in the Norma Cluster has an H$_2$/H I ratio higher than unity, necessitating numerical studies of RPS galaxies with extremely high gas fractions.

4. Hα Emission from an RPS Galaxy

A young stellar population emits the Lyman continuum (LyC) photons that ionize the surrounding gas. The ionized hydrogen subsequently recombines with electrons, producing Hα photons at 6562.8 Å. Therefore, Hα detection in RPS galaxies is often considered as an indication of star formation (e.g., Jáchym et al. 2017, 2019; Sheen et al. 2017; Yagi et al. 2017). However, Hα photons can also be produced by collisional radiation, which does not require LyC radiation from young stars. Furthermore, heating due to processes other than star formation, such as shocks or mixing, can yield Hα. Thus, in this section, we investigate the origin of Hα emission in RPS galaxies and discuss a possible way to determine SFRs from Hα in the tail.

Figure 11 shows the dust-obscured Hα SB maps of the gas-rich galaxy (`FaceWind10_rich`) at $t = 185$ and 366 Myr and the distribution of all disk stars (yellow contours), disk stars younger than 20 Myr (blue contours), and tail stars older (open gray circles) and younger (open white stars) than 20 Myr. As strong ICM winds truncate the outskirts of the gaseous disk, the star-forming region notably shrinks in the disk between the two epochs. At $t = 185$ Myr, the stellar disk is bowed owing to the gravitational interaction with the gaseous disk that is pushed by the strong ram pressure. However, the stellar disk recovers its shape once the gaseous disk is largely stripped, as seen at $t = 366$ Myr.

Most young tail stars coincide with the local Hα maxima. At $t = 185$ Myr, when the SFR in the tail peaks (Figure 5), a clump of stellar particles of $M_\star = 7.2 \times 10^4 M_\odot$ is born in the narrow region located at the interface between the tail and ICM wind, forming bright Hα cores inside the white star symbols marked by D in Figure 11. Among them, the brightest Hα core has intrinsic $F_{H\alpha} = 2.41 \times 10^{41}$ erg s^{-1} kpc^{-2}, and its

dust-obscured SB is $F_{H\alpha} = 2.11 \times 10^{38}$ erg s^{-1} kpc^{-2}. We confirm that the bright Hα pixels are formed at the position of newly formed stellar particles. In the last stage of the simulation ($t = 366$ Myr), stellar particles younger than 20 Myr are observed across the entire tail with a total mass of $M_\star = 1.8 \times 10^4 M_\odot$. The brightest Hα core in the tail has intrinsic Hα SB of 6.15×10^{40} erg s^{-1} kpc^{-2} at $t = 366$ Myr, which is only a quarter of the brightest Hα core in the tail at $t = 185$ Myr.

In Figure 12, we compare the intrinsic SFRs averaged over 20 Myr and those estimated from the total Hα luminosities in the disk and tail. To make the comparison from an observational perspective, we assume that the simulated galaxy lies at $z = 0.0173$ and is observed by the Multi Unit Spectroscopic Explorer instrument on the Very Large Telescope, with a pixel scale of 0″2. Under these conditions, each pixel has a physical scale of 0.073 kpc, assuming cosmological parameters $H_0 = 67.74$ km s^{-1} Mpc^{-1} and $\Omega_0 = 0.3089$ (Planck Collaboration et al. 2016). The Hα luminosity of the disk is measured from the pixels covering the cylindrical volume of the disk with a radius of $r = 12$ kpc and a height of $h = \pm3$ kpc from the galactic plane, as defined in Section 2.2. The Hα luminosity of the tail is similarly obtained from the pixels covering the cylindrical volume extending from the upper surface of the disk to the boundary. Then, we infer the empirical SFR, SFR$_{H\alpha}$, from the Hα SB using a simple scaling relation between the SFR and an unobscured Hα luminosity:

$$\mathrm{SFR}_{H\alpha} \approx 4.0 \, M_\odot \, \mathrm{yr}^{-1} \left(\frac{L_{H\alpha}}{10^{42} \, \mathrm{erg \, s}^{-1}} \right), \qquad (9)$$

which is appropriate for a stellar population with a metallicity of $Z = 0.01$ in BPASS (v2.0; Eldridge et al. 2008; Stanway et al. 2016).

Figure 12 shows that, in the disk, SFR$_{H\alpha}$ closely matches the intrinsic SFR within $\sim$20% error, regardless of the assumed SB limit. On the other hand, a marked difference is observed between the intrinsic SFR and SFR$_{H\alpha}$ in the tail. To determine the cause of the difference, we compute the relative
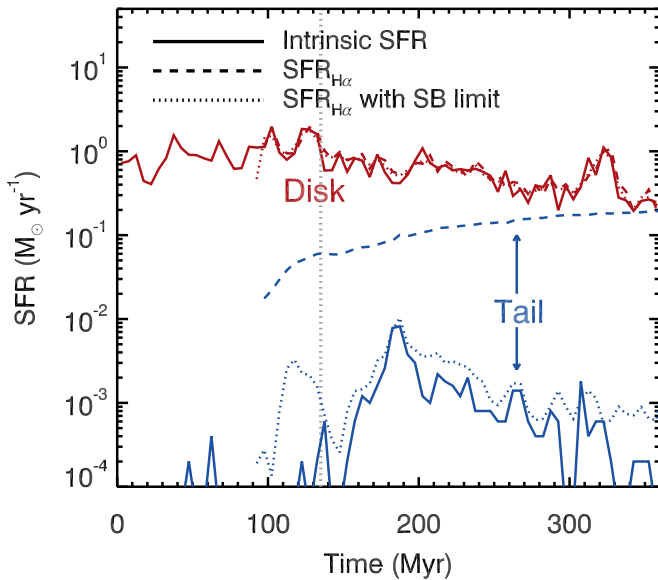
Figure 12. Evolution of the intrinsic SFR (solid) and the SFR estimated from the total unobscured Hα luminosity (SFR$_{H\alpha}$; dashed and dotted). The red and blue colors indicate the SFRs in the disk and tail, respectively. We present SFR$_{H\alpha}$ with (dotted) and without (dashed) an SB limit of 6×10^{38} erg s^{-1} kpc^{-2}. We display the SFR$_{H\alpha}$ lines only at $t > 100$ Myr. The vertical dotted line marks the epoch at which the wind front reaches the galaxy. SFR$_{H\alpha}$ closely traces the intrinsic SFR in the disk, while the majority of the Hα SB (dashed) in the tail originates from processes other than star formation. However, the intrinsic SFR in the tail is reasonably recovered by considering Hα bright regions (dotted).

Figure 13. The relation between the SFR surface density (Σ_{SFR}) and Hα SB at $t = 185$ Myr when the SFR in the tail is maximal. The disk and tail regions are denoted by orange circles and blue squares, respectively. The green squares display the relation in the tail at the final snapshot ($t = 366$ Myr). We illustrate the SFR–Hα relation expected from BPASS (Eldridge et al. 2008; Stanway et al. 2016) with a gray dashed line. The colored bars in the bottom panel indicate the SB ranges of the pixels contributing to the 1st–99th percentile distribution of the total Hα luminosities of the regions with no star formation in the tail (blue) and disk (orange). The orange circle and blue square in the colored bars mark the median values. Note that processes other than star formation lead to Hα SB of up to 6×10^{38} erg s^{-1} kpc^{-2} in the tail, indicating that the pixels with higher Hα SB are likely to be observed as star-forming regions.

contribution from collisional and recombinative transitions to the total number of Hα photons. We find that ≈90% of Hα photons in the tail are emitted from the gas with 0.01 cm^{-3} < n_H < 1 cm^{-3}, while ≈10% arises from the gas with n_H > 1 cm^{-3} during the entire time period. At n_H > 1 cm^{-3}, more than 97% of Hα photons are emitted via recombinative transition, but in the diffuse gas, collisional radiation produces twice more Hα photons than recombinative transition. Thus, we conclude that Hα in the tail is mainly powered by a process unrelated to star formation, i.e., collisional radiation (63%). The remaining Hα (37%) is also unlikely to originate directly from star formation, given that the intrinsic SFR is several orders of magnitude smaller than SFR$_{H\alpha}$. Instead, we argue that the additional Hα photons in the tail arise from the interaction with a hot ICM that heats up the diffuse gas and stimulates the recombinative as well as collisional radiation.

In principle, LyC photons that manage to escape from the galactic disk can also contribute to Hα flux in the tail. However, we confirm that the LyC flux measured in the distant tail ($z > 10$ kpc) is insufficient (≲15%) to explain the entire Hα flux. We also estimate a possible contribution from the UV background radiation by measuring Hα emission from low-density gas that is not self-shielded from the UV (n_H < 0.01 cm^{-3}; Rosdahl & Blaizot 2012). We find that the Hα photons emitted from the low-density gas account for less than 0.5% of the total Hα emission in the tail, and thus the UV background used in this study is also unlikely to power the Hα tails.

We further examine whether bright Hα blobs in the tail trace star-forming regions by correlating an intrinsic SFR and unobscured Hα SB in each pixel (which corresponds to 73 by 73 pc^2 in a physical scale) in Figure 13. The Hα SB of each pixel from the disk (orange) and tail regions (blue) is projected at $t = 185$ Myr, when the SFR peaks in the tail. Although Hα

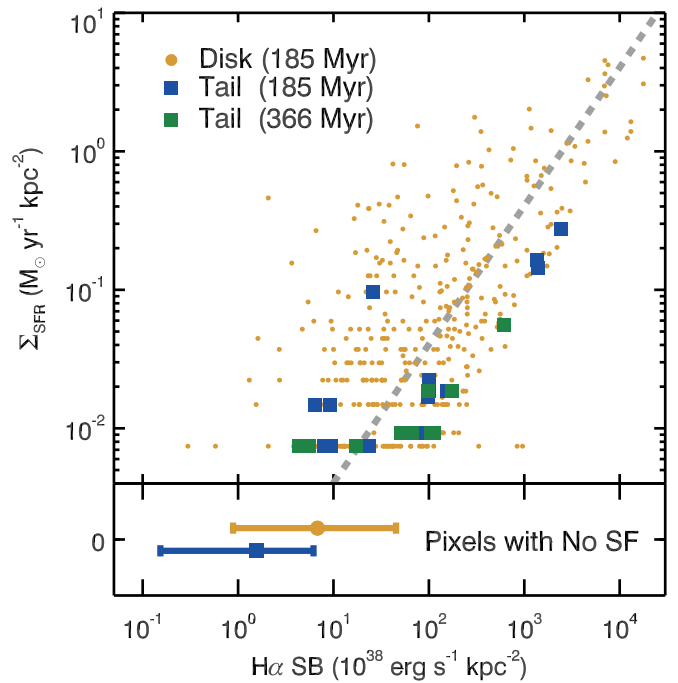SB is notably scattered at a fixed Σ_{SFR}, it follows reasonably well the predicted SFR–Hα relation (gray dashed line and Equation (9)).

For comparison, we present the SB range of the pixels contributing to the 1st–99th percentile distribution of the total Hα luminosities of the regions with no stars younger than 20 Myr, in the bottom panel. Non-star-forming regions in the disk can display pixels as bright as 10^{39} erg s^{-1} kpc^{-2}. However, the pixels in the tail with no star formation exhibit Hα SB lower than 6×10^{38} erg s^{-1} kpc^{-2}, which roughly corresponds to the typical Hα SB at the minimum Σ_{SFR} of ∼0.005 $M_\odot$ yr^{-1} kpc^{-2}. Thus, we conclude that the bright Hα blobs in the tail are lit by nearby young stars. Additionally, our experiments suggest that the detection of the Hα emission brighter than 6×10^{38} erg s^{-1} kpc^{-2} can be considered as a sign of star formation in the RPS tail, while the well-developed tail structures with Hα SB < 10^{38} erg s^{-1} kpc^{-2}, observed in, e.g., ESO 137-001 (Fumagalli et al. 2014), are likely to be induced by processes other than star formation. Thus, the discrepancy between the intrinsic SFR and SFR$_{H\alpha}$ in the tail is alleviated if a high SB limit is applied to include actual star-forming sites (e.g., 6×10^{38} erg s^{-1} kpc^{-2}), as shown by the dotted line in Figure 12.

5. X-Ray-to-Hα Flux Ratio and Mixing

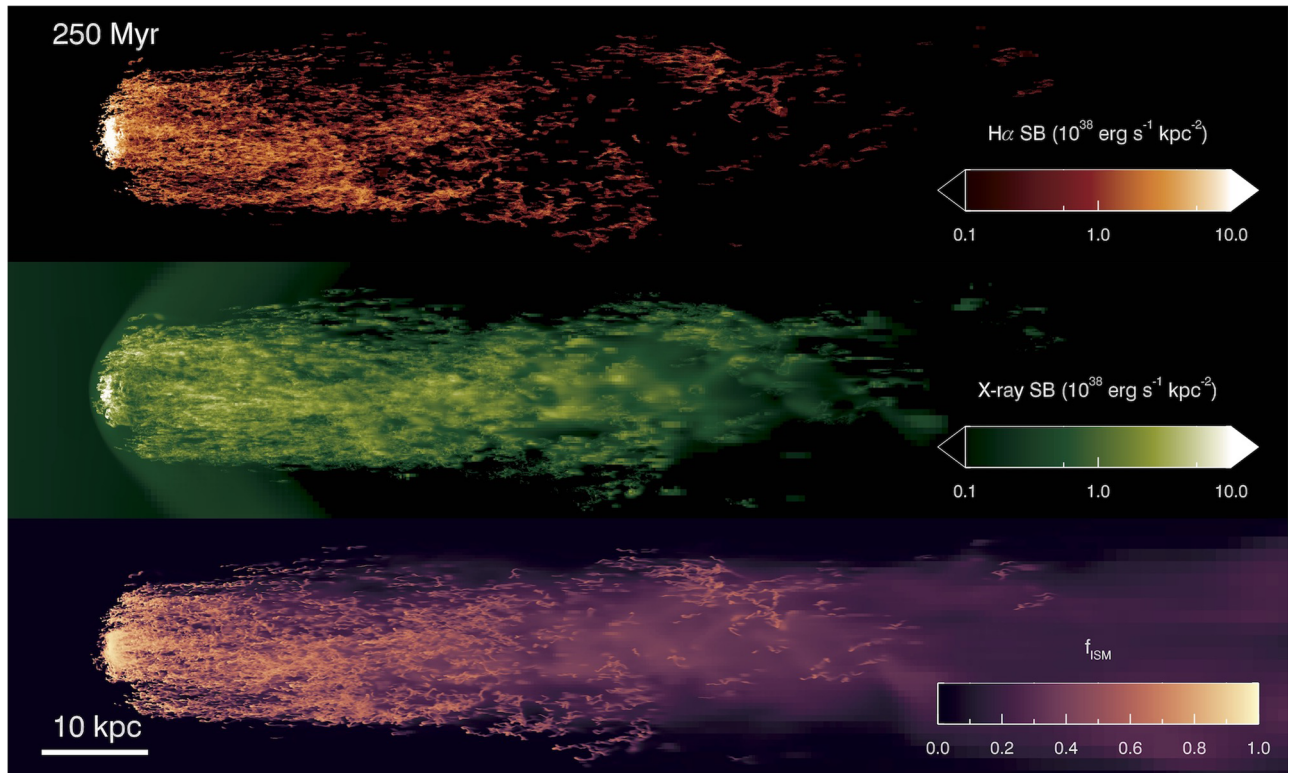In addition to Hα emission, RPS tails are often detected in X-rays (Finoguenov et al. 2004; Wang et al. 2004; Machacek

Figure 14. Dust-obscured Hα SB (top), X-ray SB in the energy band [0.4, 7.5] keV (i.e., before the bolometric correction; middle), and ISM fraction of the gas-rich galaxy at $t = 250$ Myr (bottom) when the length of the tail is comparable to that of ESO 137-001 and D100.

et al. 2005; Sun & Vikhlinin 2005; Sun et al. 2006, 2010; Poggianti et al. 2019). Since X-ray photons are preferentially produced by hot plasma with $T \sim 10^7$ K, the coexistence of Hα and X-ray suggests a complex thermal structure of the RPS tail. Furthermore, Sun et al. (2021) recently argued that the flux ratio of X-ray to Hα ($F_X/F_{H\alpha}$) may be used as a signature of the ICM–ISM interaction (see also Poggianti et al. 2019). They showed that galactic disks typically have $F_X/F_{H\alpha} \lesssim 0.4$, but the RPS tails exhibit a high $F_X/F_{H\alpha}$ of 3–4, likely because of the mixing between the ICM and ISM (e.g., Tonnesen et al. 2011).

To understand the mixing process and to gauge whether the Hα-to-X-ray flux ratio can be used as an indication of mixing, we generate mock X-ray SB maps of the RPS galaxy using the YT package (Turk et al. 2011). The X-ray emissivity is estimated as

$$\epsilon_X = n_{H\,II} n_e [\Lambda_{X,p}(T) + \Lambda_{X,m}(T, Z)], \qquad (10)$$

where $\Lambda_{X,p}$ and $\Lambda_{X,m}$ are the X-ray cooling functions for primordial gas and metals, respectively, taken from the Astrophysical Plasma Emission Code (APEC; Smith et al. 2001). Following the bolometric correction procedure by Sun et al. (2021), we first compute the X-ray emissivity in the [0.4, 7.5] keV energy band and derive the bolometric flux using conversion factors measured from APEC as a function of temperature. The model bolometric correction factor at temperature T is defined as $c_{bol}(T) \equiv L_{X,bol}(T)/L_{X,[0.4,7.5]\,keV}(T)$, where $L_{X,bol}(T)$ is the model bolometric luminosity and $L_{X,[0.4,7.5]\,keV}(T)$ is the model luminosity at [0.4, 7.5] keV. X-ray emissivity-weighted temperature is used in the calculation of the correction factor. Because we mimic the ICM wind by

imposing a boundary condition of high temperature ($T = 10^7$ K), the ICM wind itself produces an X-ray background of $\sim 5 \times 10^{37}$ erg s^{-1} kpc^{-2}. The background X-ray emission is removed by subtracting the X-ray SB profiles averaged at the boundary of the simulation box, similar to observations.

Figure 14 exhibits the maps of dust-obscured Hα SB (top), X-ray SB (middle), and the mass fraction of the gas originating from the ISM (f_{ISM}; bottom) in the gas-rich galaxy at $t = 250$ Myr. We select this snapshot because the simulated RPS tail extends out to ~ 80 kpc, which is comparable to that of ESO 137-001 in the Norma Cluster (Sun et al. 2021) and D100 in the Coma Cluster (Jáchym et al. 2017). The X-ray SB and ISM fraction maps clearly indicate the presence of hot diffuse clouds mixed with the stripped ISM in the tail ($T \sim 10^6$ K and $n_H \sim 0.01$ cm^{-3}). Such gas is bright in X-ray but is faint in Hα because of the high temperatures (see, e.g., the tail region at 30–40 kpc in Figure 14). Conversely, Hα bright clouds in the tails at $z > 10$ kpc are cooler ($T \sim 10^4$ K) and denser ($n_H \sim 0.1$ cm^{-3}), and their contribution to the total X-ray luminosity is minor.

To understand the relationship between the flux ratio ($F_X/F_{H\alpha}$) and the mixing, we sample the SB maps in the `FaceWind10_rich` run at $t = 250$ Myr with 0.2×0.2 kpc^2 pixels (top panel) or 10×10 kpc^2 pixels (bottom panel) in Figure 15. The measurements on 1×1 kpc^2 pixels for the galactic disk at $|z| < 3$ kpc are also presented as blue contours in the bottom panel. The black dashed line ($F_X/F_{H\alpha} = 3.48$) corresponds to the empirical fit to the 16 observed tails of the Virgo, Coma, A1367, and A3627 Cluster galaxies (see Sun et al. 2021, for further details). The light-blue shade marks the approximate range of the empirical SB ratio of the galactic disk also taken from Sun et al. (2021). Since no extinction
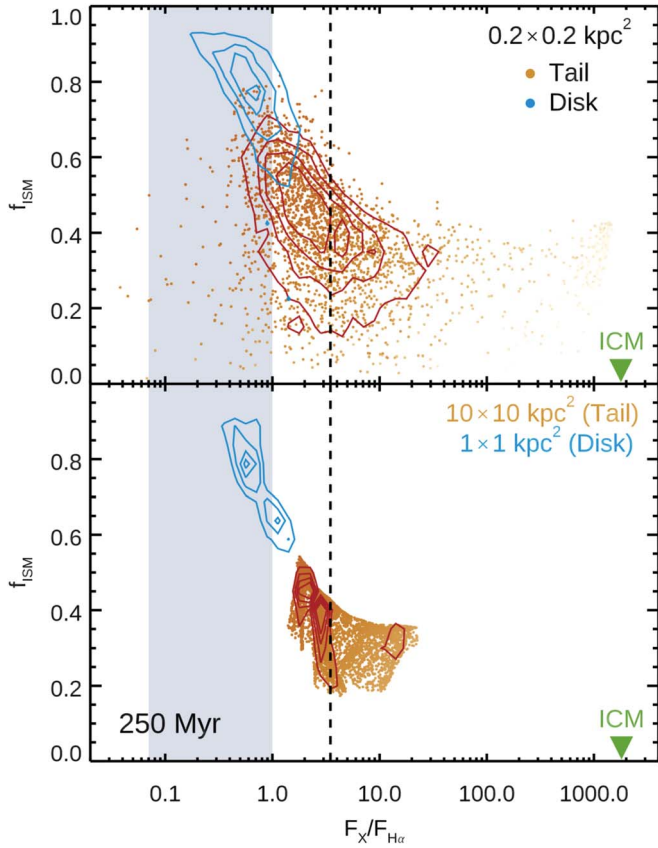
Figure 15. The correlation between $f_{\rm ISM}$ and the flux ratio of X-ray to dust-obscured Hα in the disk (cyan contours) and RPS tail (orange dots and red contours) of the `FaceWind10_rich` galaxy at $t = 250$ Myr. The flux ratio of the imposed ICM wind is shown as green triangles. Darker orange dots correspond to the tail regions with brighter Hα. We compute the SB in pixels with area 0.2×0.2 kpc^2 in the top panel, while larger pixels are used for the tail (10×10 kpc^2) or for the disk region (1×1 kpc^2) in the bottom panel. The light-blue shaded regions and vertical dashed lines indicate the observed $F_{\rm X}/F_{\rm H\alpha}$ in the disk and RPS tail (Sun et al. 2021), respectively.

corrections are applied to the Hα SB of the diffuse tails in Sun et al. (2021), we also use the dust-obscured Hα SB maps.[9]

We find that the galactic disks form a distinctive sequence in Figure 15, with the flux ratio $F_{\rm X}/F_{\rm H\alpha} \lesssim 1.5$, consistent with the observations (Sun et al. 2021). The mean flux ratio of the simulated disk tends to be slightly larger than the average observed ratio, which is likely due to the boosted SN feedback employed in this work. In contrast, the pure ICM gas shows a higher $F_{\rm X}/F_{\rm H\alpha}$ of ~ 1800 (the green triangles in Figure 15). The mixing of the ISM into the ICM leads to the decrease of the hot gas temperature, and thus X-ray emissivity is reduced while Hα becomes brighter with increasing $f_{\rm ISM}$. Consequently, the ICM-dominant tail gas shows $F_{\rm X}/F_{\rm H\alpha} \sim 1$–$100$, while the gas in the disk vicinity ($3\,{\rm kpc} < z < 10\,{\rm kpc}$) exhibits a lower $F_{\rm X}/F_{\rm H\alpha}$ of ~ 1. This is again compatible with the observed trend that $F_{\rm X}/F_{\rm H\alpha}$ tends to increase for distant tails (Sun et al. 2021). Therefore, we argue that the intermediate SB ratio observed in the RPS tail can be seen as a sign of ICM–ISM mixing (Tonnesen et al. 2011).

We also remark that the predicted flux ratios in the tail ($F_{\rm X}/F_{\rm H\alpha} \sim 1.5$–$3.5$) are slightly smaller than those

---

[9] However, we note that attenuation due to dust in our simulated tail is negligible because the tail gas is highly ionized and a large amount of dust is destroyed (see Equation (8)).

observed ($F_{\rm X}/F_{\rm H\alpha} = 3.48$; Sun et al. 2021). Given that a large amount of dust in the relatively hot tail gas is unlikely to survive and reduce $F_{\rm H\alpha}$, it is more probable that the X-ray fluxes in the tail are underestimated. The correlation between $f_{\rm ISM}$ and $F_{\rm X}/F_{\rm H\alpha}$ in Figure 15 then suggests that the ICM should be mixed with the ISM more efficiently in the tail. This may be achieved by including thermal conduction (e.g., Armillotta et al. 2017; Li et al. 2020) and/or by resolving hydrodynamic instabilities with higher resolution.

Finally, it is also worth pointing out that the flux ratios in the simulated tail are widely distributed on small scales (0.1 kpc), while they tend to converge to ~ 1 when sampled on kiloparsec scales. This suggests that the difference in the flux ratio between the disk and RPS tails found by Sun et al. (2021) may be less dramatic if high-resolution observational data are obtained.

6. Conclusions

We investigated the formation of jellyfish galaxies using a set of idealized simulations for a dwarf-sized galaxy with a multiphase ISM in environments with and without strong ICM winds devised to mimic the ram pressure at a cluster center. As a follow-up study of L20, we adopted the same code, physics, simulation setup, and initial condition as those of L20, but with a raised initial gas fraction. We primarily focused on the formation process of multiphase clouds and stars in RPS tails. We found that the mixing of a stripped ISM with the ICM is a key process determining the characteristics of a jellyfish galaxy. Our results are summarized as follows:

1. Strong ram pressure efficiently suppresses star formation in the disk of a gas-rich galaxy by truncating the outskirts of the gaseous disk, which is consistent with the prediction of Gunn et al. (1972). The decaying trends in SFRs in the galactic disk are similar for the `FaceWind10_rich` and `FaceWind10` galaxies, in spite of their different initial gas fractions ($M_{\rm H\,I}/M_\star = 4.1$ versus 0.8).

2. Molecular gas can form in situ in the distant RPS tail of the `FaceWind10_rich` galaxy. The stripped ISM is mixed with the ICM, enhancing the formation of warm ionized gas in the RPS tail. Half of the H II clouds with $f_{\rm ICM} > 0.5$ have cooling timescales shorter than a few Myr in `FaceWind10_rich`, which is in contrast to the results of the `FaceWind10` galaxy, because of the lack of stripped ISM. This indicates that the stripping of a large amount of ISM plays a critical role in the formation of molecular clouds in RPS tails.

3. The RPS tails in the `FaceWind10_rich` galaxy form stars at a rate of $1.2 \times 10^{-3}\,M_\odot\,{\rm yr}^{-1}$ on average after the galaxy encounters the ICM wind. The majority of the tail stars are initially formed in the stripped wake within 10 kpc from the galactic plane, but a small amount of stars ($8 \times 10^3\,M_\odot$) also forms in the distant tail ($z > 60$ kpc) ~ 200 Myr after the galaxy starts to interact with the ICM wind. Stars in the distant tail form out of molecular clumps that are composed of gas that is a mixture of stripped ISM and the ambient ICM ($f_{\rm ISM} \sim 0.5$).

4. The intrinsic SFR in the disk is reasonably recovered from the Hα emission. In the RPS tail, only bright Hα cores trace actual star-forming regions. Hα emission

below $6 \times 10^{38} \, \mathrm{erg \, s^{-1} \, kpc^{-2}}$ can originate from processes other than star formation, and the high SB limit needs to be imposed to recover the intrinsic SFR from Hα in the simulated RPS tail.

5. A strong correlation is present between the ISM fraction and the flux ratio of X-ray to Hα ($F_X/F_{H\alpha}$) in `FaceWind10_rich`. The typical flux ratio in the RPS tail ($1.5 \lesssim F_X/F_{H\alpha} \lesssim 20$) is higher than that of the galactic disk ($F_X/F_{H\alpha} \lesssim 1.5$) and lower than that of the ICM gas ($F_X/F_{H\alpha} \sim 1800$) when measured on $10 \times 10 \, \mathrm{kpc^2}$ scales. Although a factor of two difference is seen between the tail $F_X/F_{H\alpha}$ of our model and the empirical fit of Sun et al. (2021), the trend still clearly supports the interpretation that the observed intermediate flux ratio indicates the mixing between the ISM and ICM.

We have shown that several RPS features can be reproduced when a large amount of ISM material is stripped from a gas-rich galaxy via strong ram pressure, forming prominent multiphase tails due to mixing with a hot ambient medium. However, several issues still need to be addressed in future studies. First, thermal conduction is not included in this work. Li et al. (2020) examine the effects of radiative cooling, self-shielding, self-gravity, magnetic field, and Braginskii conduction and viscosity and show that cooling and conduction are the physical processes that govern the lifetime of cool clouds in a circumgalactic medium. In their study, conduction efficiently evaporates small clouds that are weakly or not at all self-shielded, while it hardly affects cool and dense clumps. This suggests that conduction could suppress the growth of cold clumps in the RPS tail. Second, our simulations do not include explicit viscosity. Roediger et al. (2015b) demonstrate that the mixing becomes less efficient with increasing viscosity in the RPS tails. Li et al. (2020) also show that a boundary layer formed by viscosity can insulate the stripped ISM from the ICM, increasing the lifetime of the cool clouds. Although it is clear that viscosity plays a role in the mixing process, we note that strong viscosity effects would suppress X-ray emissivity in the tail, potentially aggravating the agreement seen in $F_X/F_{H\alpha}$ (Figure 15). If this is really the case, the viscosity effects should be offset by other processes, such as conduction (Li et al. 2020). Third, we assume a constant ICM wind in this work, but galaxies orbiting around the real cluster would undergo ram pressure that changes over time (e.g., Roediger & Brüggen 2007; Roediger et al. 2015a; Jung et al. 2018; Yun et al. 2019). For example, Tonnesen (2019) shows that the gas stripping rates and tail sizes become smaller if the wind strengths are gradually increased, compared to the run with constant winds. In this regard, the impact of the ram pressure in our simulations may be overestimated, perhaps enhancing the star formation in the RPS tail. Fourth, we neglect UV radiation from active galactic nuclei (AGNs) or star-forming brightest cluster galaxies (Hicks et al. 2010; Klesman & Sarajedini 2012; Fogarty et al. 2015; Poggianti et al. 2017) in a cluster environment. These sources can provide extra heating, potentially limiting star formation in the RPS tail. Unfortunately, the effect of the stronger UV radiation depends on (variable) AGN or star formation activity, which is difficult to estimate without performing realistic simulations. Last but not the least, our simulations still do not explain some key properties of observed RPS tails. For example, the D100 tail in the Coma Cluster is observed to have SFRs comparable with or only a factor of a few higher than that of the

`FaceWind10_rich` galaxy, but the amount of molecular clouds is 10 times larger than that in `FaceWind10_rich`. Even more intriguing is the H I deficiency in the D100 and ESO 137-001 tails (Jáchym et al. 2014, 2017, 2019), indicating that RPS gas may turn into molecular clouds very efficiently in certain conditions. These issues necessitate future studies probing a larger parameter space and physical ingredients in realistic cluster environments.

ORCID iDs

Jaehyun Lee https://orcid.org/0000-0002-6810-1778
Taysun Kimm https://orcid.org/0000-0002-3950-3997
Jérémy Blaizot https://orcid.org/0000-0003-1609-7911
Harley Katz https://orcid.org/0000-0003-1561-3814
Wonki Lee https://orcid.org/0000-0002-1566-5094
Yun-Kyeong Sheen https://orcid.org/0000-0002-3211-9431
Julien Devriendt https://orcid.org/0000-0002-8140-0422

References

Armillotta, L., Fraternali, F., & Marinacci, F. 2016, MNRAS, 462, 4157
Armillotta, L., Fraternali, F., Werk, J. K., Prochaska, J. X., & Marinacci, F. 2017, MNRAS, 470, 114
Asplund, M., Grevesse, N., Sauval, A. J., & Scott, P. 2009, ARA&A, 47, 481
Bekki, K., & Couch, W. J. 2003, ApJL, 596, L13
Blitz, L., & Shu, F. H. 1980, ApJ, 238, 148
Boselli, A., Cuillandre, J. C., Fossati, M., et al. 2016, A&A, 587, A68
Boselli, A., & Gavazzi, G. 2006, PASP, 118, 517
Bravo-Alfaro, H., Cayatte, V., van Gorkom, J. H., & Balkowski, C. 2000, AJ, 119, 580
Bravo-Alfaro, H., Cayatte, V., van Gorkom, J. H., & Balkowski, C. 2001, A&A, 379, 347
Burgess, A., & Tully, J. A. 1992, A&A, 254, 436
Catinella, B., Saintonge, A., Janowiecki, S., et al. 2018, MNRAS, 476, 875
Chung, A., van Gorkom, J. H., Kenney, J. D. P., Crowl, H., & Vollmer, B. 2009, AJ, 138, 1741
Chung, A., van Gorkom, J. H., Kenney, J. D. P., & Vollmer, B. 2007, ApJL, 659, L115
Cortese, L., Gavazzi, G., Boselli, A., et al. 2006, A&A, 453, 847
Cortese, L., Marcillac, D., Richard, J., et al. 2007, MNRAS, 376, 157
Davies, R. D., & Lewis, B. M. 1973, MNRAS, 165, 231
Del Zanna, G., Dere, K. P., Young, P. R., & Landi, E. 2021, ApJ, 909, 38

Dere, K. P., Del Zanna, G., Young, P. R., Landi, E., & Sutherland, R. S. 2019, ApJS, 241, 22
Dere, K. P., Landi, E., Mason, H. E., Monsignori Fossi, B. C., & Young, P. R. 1997, A&AS, 125, 149
Ebeling, H., Stephenson, L. N., & Edge, A. C. 2014, ApJL, 781, L40
Eldridge, J. J., Izzard, R. G., & Tout, C. A. 2008, MNRAS, 384, 1109
Ferland, G. J., Korista, K. T., Verner, D. A., et al. 1998, PASP, 110, 761
Finoguenov, A., Briel, U. G., Henry, J. P., et al. 2004, A&A, 419, 47
Fogarty, K., Postman, M., Connor, T., Donahue, M., & Moustakas, J. 2015, ApJ, 813, 117
Fossati, M., Gavazzi, G., Boselli, A., & Fumagalli, M. 2012, A&A, 544, A128
Franchetto, A., Tonnesen, S., Poggianti, B. M., et al. 2021, ApJL, 922, L6
Fumagalli, M., Fossati, M., Hau, G. K. T., et al. 2014, MNRAS, 445, 4335
Garel, T., Blaizot, J., Rosdahl, J., et al. 2021, MNRAS, 504, 1902
Gavazzi, G., Boselli, A., Mayer, L., et al. 2001, ApJL, 563, L23
George, K., Poggianti, B. M., Gullieuszik, M., et al. 2018, MNRAS, 479, 4126
Grishin, K. A., Chilingarian, I. V., Afanasiev, A. V., et al. 2021, NatAs, 5, 1308
Gronke, M., & Oh, S. P. 2018, MNRAS, 480, L111
Guillet, T., & Teyssier, R. 2011, JCoPh, 230, 4756
Gunn, J. E., Gott, J., & Richard, I. 1972, ApJ, 176, 1
Halle, A., & Combes, F. 2013, A&A, 559, A55
Hicks, A. K., Mushotzky, R., & Donahue, M. 2010, ApJ, 719, 1844
Hollenbach, D., & McKee, C. F. 1979, ApJS, 41, 555
Hudson, D. S., Mittal, R., Reiprich, T. H., et al. 2010, A&A, 513, A37
Hui, L., & Gnedin, N. Y. 1997, MNRAS, 292, 27
Jáchym, P., Combes, F., Cortese, L., Sun, M., & Kenney, J. D. P. 2014, ApJ, 792, 11
Jáchym, P., Kenney, J. D. P., Sun, M., et al. 2019, ApJ, 883, 145
Jáchym, P., Köppen, J., Palouš, J., & Combes, F. 2009, A&A, 500, 693
Jáchym, P., Sun, M., Kenney, J. D. P., et al. 2017, ApJ, 839, 114
Jung, S. L., Choi, H., Wong, O. I., et al. 2018, ApJ, 865, 156
Kapferer, W., Kronberger, T., Ferrari, C., Riser, T., & Schindler, S. 2008, MNRAS, 389, 1405
Kapferer, W., Sluka, C., Schindler, S., Ferrari, C., & Ziegler, B. 2009, A&A, 499, 87
Katz, H., Kimm, T., Sijacki, D., & Haehnelt, M. G. 2017, MNRAS, 468, 4831
Kenney, J. D. P., van Gorkom, J. H., & Vollmer, B. 2004, AJ, 127, 3361
Kim, C.-G., & Ostriker, E. C. 2018, ApJ, 853, 173
Kimm, T., Cen, R., Devriendt, J., Dubois, Y., & Slyz, A. 2015, MNRAS, 451, 2900
Kimm, T., Katz, H., Haehnelt, M., et al. 2017, MNRAS, 466, 4826
Klesman, A. J., & Sarajedini, V. L. 2012, MNRAS, 425, 1215
Koopmann, R. A., & Kenney, J. D. P. 2004a, ApJ, 613, 851
Koopmann, R. A., & Kenney, J. D. P. 2004b, ApJ, 613, 866
Kronberger, T., Kapferer, W., Ferrari, C., Unterguggenberger, S., & Schindler, S. 2008, A&A, 481, 337
Kroupa, P. 2001, MNRAS, 322, 231
Kubo, J. M., Stebbins, A., Annis, J., et al. 2007, ApJ, 671, 1466
Laudari, S., Jáchym, P., Sun, M., et al. 2022, MNRAS, 509, 3938
Laursen, P., Sommer-Larsen, J., & Andersen, A. C. 2009, ApJ, 704, 1640
Lee, B., & Chung, A. 2018, ApJL, 866, L10
Lee, B., Chung, A., Tonnesen, S., et al. 2017, MNRAS, 466, 1382
Lee, J., Kimm, T., Katz, H., et al. 2020, ApJ, 905, 31
Li, H., Gnedin, O. Y., & Gnedin, N. Y. 2018, ApJ, 861, 107
Li, Z., Hopkins, P. F., Squire, J., & Hummels, C. 2020, MNRAS, 492, 1841
Łokas, E. L., & Mamon, G. A. 2003, MNRAS, 343, 401
Machacek, M., Dosaj, A., Forman, W., et al. 2005, ApJ, 621, 663
Mohr, J. J., Mathiesen, B., & Evrard, A. E. 1999, ApJ, 517, 627
Moretti, A., Paladino, R., Poggianti, B. M., et al. 2018, MNRAS, 480, 2508
Mun, J. Y., Hwang, H. S., Lee, M. G., et al. 2021, JKAS, 54, 17
Navarro, J. F., Frenk, C. S., & White, S. D. M. 1996, ApJ, 462, 563
Oosterloo, T., & van Gorkom, J. 2005, A&A, 437, L19
Ostriker, E. C., McKee, C. F., & Leroy, A. K. 2010, ApJ, 721, 975

Owers, M. S., Couch, W. J., Nulsen, P. E. J., & Randall, S. W. 2012, ApJL, 750, L23
Planck Collaboration, Ade, P. A. R., Aghanim, N., et al. 2016, A&A, 594, A13
Poggianti, B. M., Fasano, G., Omizzolo, A., et al. 2016, AJ, 151, 78
Poggianti, B. M., Ignesti, A., Gitti, M., et al. 2019, ApJ, 887, 155
Poggianti, B. M., Moretti, A., Gullieuszik, M., et al. 2017, ApJ, 844, 48
Ramos-Martínez, M., Gómez, G. C., & Pérez-Villegas, Á. 2018, MNRAS, 476, 3781
Rawle, T. D., Altieri, B., Egami, E., et al. 2014, MNRAS, 442, 196
Roediger, E., & Brüggen, M. 2006, MNRAS, 369, 567
Roediger, E., & Brüggen, M. 2007, MNRAS, 380, 1399
Roediger, E., & Brüggen, M. 2008, MNRAS, 388, 465
Roediger, E., Kraft, R. P., Nulsen, P. E. J., et al. 2015a, ApJ, 806, 103
Roediger, E., Kraft, R. P., Nulsen, P. E. J., et al. 2015b, ApJ, 806, 104
Rosdahl, J., & Blaizot, J. 2012, MNRAS, 423, 344
Rosdahl, J., Blaizot, J., Aubert, D., Stranex, T., & Teyssier, R. 2013, MNRAS, 436, 2188
Rosdahl, J., Katz, H., Blaizot, J., et al. 2018, MNRAS, 479, 994
Rosdahl, J., Schaye, J., Teyssier, R., & Agertz, O. 2015, MNRAS, 451, 34
Rosdahl, J., & Teyssier, R. 2015, MNRAS, 449, 4380
Rosen, A., & Bregman, J. N. 1995, ApJ, 440, 634
Ruszkowski, M., Brüggen, M., Lee, D., & Shin, M. S. 2014, ApJ, 784, 75
Schulz, S., & Struck, C. 2001, MNRAS, 328, 185
Scott, T. C., Bravo-Alfaro, H., Brinks, E., et al. 2010, MNRAS, 403, 1175
Scott, T. C., Brinks, E., Cortese, L., Boselli, A., & Bravo-Alfaro, H. 2018, MNRAS, 475, 4648
Scott, T. C., Cortese, L., Brinks, E., et al. 2012, MNRAS, 419, L19
Sheen, Y.-K., Smith, R., Jaffé, Y., et al. 2017, ApJL, 840, L7
Shin, M.-S., & Ruszkowski, M. 2014, MNRAS, 445, 1997
Smith, R. K., Brickhouse, N. S., Liedahl, D. A., & Raymond, J. C. 2001, ApJL, 556, L91
Stanway, E. R., Eldridge, J. J., & Becker, G. D. 2016, MNRAS, 456, 485
Steinhauser, D., Haider, M., Kapferer, W., & Schindler, S. 2012, A&A, 544, A54
Storey, P. J., & Hummer, D. G. 1995, MNRAS, 272, 41
Sun, M., Donahue, M., Roediger, E., et al. 2010, ApJ, 708, 946
Sun, M., Ge, C., Luo, R., et al. 2021, NatAs, 6, 270
Sun, M., Jones, C., Forman, W., et al. 2006, ApJL, 637, L81
Sun, M., Jones, C., Forman, W., et al. 2007, ApJ, 657, 197
Sun, M., & Vikhlinin, A. 2005, ApJ, 621, 718
Teyssier, R. 2002, A&A, 385, 337
Tonnesen, S. 2019, ApJ, 874, 161
Tonnesen, S., & Bryan, G. L. 2012, MNRAS, 422, 1609
Tonnesen, S., & Bryan, G. L. 2021, ApJ, 911, 68
Tonnesen, S., Bryan, G. L., & Chen, R. 2011, ApJ, 731, 98
Tonnesen, S., & Stone, J. 2014, ApJ, 795, 148
Tormen, G., Moscardini, L., & Yoshida, N. 2004, MNRAS, 350, 1397
Toro, E. F., Spruce, M., & Speares, W. 1994, ShWav, 4, 25
Turk, M. J., Smith, B. D., Oishi, J. S., et al. 2011, ApJS, 192, 9
Urban, O., Werner, N., Allen, S. W., Simionescu, A., & Mantz, A. 2017, MNRAS, 470, 4583
Vázquez-Semadeni, E., Kim, J., Shadmehri, M., & Ballesteros-Paredes, J. 2005, ApJ, 618, 344
Verdugo, C., Combes, F., Dasyra, K., Salomé, P., & Braine, J. 2015, A&A, 582, A6
Vollmer, B., Cayatte, V., Balkowski, C., & Duschl, W. J. 2001, ApJ, 561, 708
Vollmer, B., Soida, M., Otmianowska-Mazur, K., et al. 2006, A&A, 453, 883
Vulcani, B., Poggianti, B. M., Gullieuszik, M., et al. 2018, ApJL, 866, L25
Wang, Q. D., Owen, F., & Ledlow, M. 2004, ApJ, 611, 821
Weingartner, J. C., & Draine, B. T. 2001, ApJ, 548, 296
Yagi, M., Komiyama, Y., Yoshida, M., et al. 2007, ApJ, 660, 1209
Yagi, M., Yoshida, M., Gavazzi, G., et al. 2017, ApJ, 839, 65
Yagi, M., Yoshida, M., Komiyama, Y., et al. 2010, AJ, 140, 1814
Yun, K., Pillepich, A., Zinger, E., et al. 2019, MNRAS, 483, 1042